1 ***Revision 1***

2 Color Effects of Cu Nanoparticles in Cu-bearing Plagioclase Feldspars

3 Word Count: 9652

4 Shiyun Jin[1], Ziyin Sun[1] and Aaron C. Palke[1]

5 [1]Gemological Institute of America, 5355 Armada Drive, Carlsbad, California 92008, U.S.A.

6 **Abstract**

7 The optical properties (scattering, absorption and extinction) of spheroidal Cu particles
8 embedded in intermediate plagioclase feldspar are computed for various sizes and shapes using
9 the Mie theory and T-matrix method. The observed color for Cu-bearing plagioclase, as a
10 function of particle size and shape, is also calculated from the computed extinction spectra. The
11 colors and pleochroism observed in natural and treated Cu-bearing plagioclase can be explained
12 from the computational results. The enigmatic green colors in some precious Oregon sunstones
13 are resulting from red light being scattered away by the Cu nanoparticles of certain sizes. The
14 UV-VIS spectra are collected on Cu-bearing plagioclase samples for comparison with the
15 computational results, which are shown to match the optical observations. The results from this
16 work may be used to quantify the concentration of colloidal Cu in plagioclase, or glass with
17 similar refractive index. Particle sizes and shapes can also be characterized using the extinction
18 and scattering spectra, which can be collected with different optical configurations. New
19 materials with special color effects and optical characteristics may be designed and engineered
20 by applying the unusual properties of metal colloids.

21 **Keywords** Oregon sunstone, Cu nanoparticle, pleochroism, absorption, scattering, extinction.

Introduction

The renowned Oregon sunstone got its name from the aventurescence effect produced by the oriented copper platelets in the clear basaltic labradorite phenocrysts (Anderson 1917; Rossman 2011). However, the most precious labradorites from Oregon are those with vivid red or green colors but no visible flaky inclusions (also called Oregon sunstone in the gemstone trade). It is well understood that colloidal Cu can produce red color by absorbing light below 600 nm. In fact, copper and gold nanoparticles have been used to produce red glass (often known as copper/gold ruby glass) for centuries (Freestone 1987; Brun et al. 1991; Nakai et al. 1999; Freestone et al. 2007; Ruivo et al. 2008; Drünert et al. 2018; Bandiera et al. 2019). The Cu in many gem feldspars on the market was actually artificially diffused into the crystals to produce the desired colors, creating huge controversy regarding the origin and authenticity of these semi-precious gemstones (Rossman 2011). Although the red color found in Oregon sunstones and other Cu-containing feldspars can be easily explained by the optical properties of Cu colloid (Hofmeister and Rossman 1985), the scarcer green color, on the other hand, is much more puzzling, since no glass counterpart with similar colors has been manufactured. Hofmeister and Rossman (1983) first hypothesized that anisotropic colloids could be associated with the pleochroism often observed in green Oregon sunstones, but also speculated that Cu^{1+}/Cu^{0} intervalence charge transfer (IVCT) or Cu^{0} pairs may be causing the green colors (Hofmeister and Rossman 1985). Farfan and Xu (2008) reported some correlation between the Cu particle orientations and the pleochroism in Oregon Sunstone. A recent TEM study has discovered anisotropic Cu nanoparticles in a pleochroic Oregon sunstone (Wang et al. 2019), which further suggests that the green colors in Oregon sunstone may also be from colloidal Cu.

Most colored stones are homogeneous solutions of light-absorbing elements or point defects, whereas the feldspars containing Cu nanoparticles (Cu-sunstones) are colloid suspensions. A transparent colloid suspension is often indistinguishable from a colored solution under ambient lighting conditions, and can only be identified using the Tyndall effect with intense and directional illumination (i.e. a laser beam). The Cu particles attenuate the light entering the feldspar crystals through both absorption and scattering, creating colors in the transmitted light (Figure 1). Only the transmittance can be easily measured using a UV-VIS spectrometer, which is used to calculate the total extinction (absorption + scattering, also called attenuation). It is impossible to measure the absorbance alone using a regular spectrometer, which means all

previously published absorption spectra (Hofmeister and Rossman 1983, 1985; Rossman 2011) of Cu-sunstones are actually extinction (attenuation) spectra, with the assumption of zero scattering. Some recent studies (Kalenskii et al. 2015; Drünert et al. 2018), however, show that the scattering cross-section of Cu nanoparticle contributes significantly to the total extinction and cannot be ignored. The light scattered by a dilute colloid suspension in any particular direction (a tiny fraction of the total scattered light) is extremely weak and may be easily neglected. Measurement of the scattered spectrum is also very difficult, because the scattered light, often anisotropic, is attenuated before leaving the crystal (by other particles and the matrix), and can be easily overwhelmed by any background noise (reflection from the instrument parts or internal reflection from the crystal facets). On the other hand, the scattered light may also contribute to the observed color (orientation dependent) in thicker crystals with higher particle concentrations, making the color effect of the Cu-sunstones even more complicated to understand.

Theoretical studies on the optical properties of submicron particles have been an important topic of physics for over a century, due to its importance in chemistry, biology, material optics, atmospheric and environmental science, remote sensing, and even astronomy. The scattering and absorption of light by a single spherical particle in a homogeneous matrix was solved analytically by Gustav Mie (1908) more than a century ago, which can be applied to dispersedly distributed spherical particles of identical size. Richard Gans (1912, 1915) extended Mie's solution for spheroidal particles much smaller than the excitation wavelength. Most real world systems of submicron particles, however, involve particles of less symmetrical shapes and distributed sizes over a wide range. The computational power required to numerically model these systems increase exponentially with the complexity of such systems. Many different methods have been developed to simulate the interaction of electromagnetic radiation with submicron particles of various shapes and sizes, such as the T-Matrix method, discrete-dipole approximation, the finite-element method and the finite-difference time-domain method, each with its own advantages and disadvantages (Wriedt 2009; Parsons et al. 2010).

Earlier calculations of the absorption spectra for copper and other metallic nanoparticles (Doremus 1964; Doremus and Turkalo 1976; Papavassiliou 1979; Ruppin 1986; Doremus et al. 1992) were mostly based on the small-size ($R \ll \lambda$) approximation of the Mie theory or the Gans theory. However, as pointed out by Hutter and Fendler (2004), the extinction cross-section of larger nanoparticles ($\varnothing > 30$ nm) is dominated by higher-order multipole absorption and

scattering, for which more complete solutions of Maxwell's equations are needed to model the extinction spectra. The optical properties of spherical copper nanoparticles in glass have only been accurately modeled very recently with the complete Mie theory (Kalenskii et al. 2015; Drünert et al. 2018), with the results compared to both archaeological and modern glass samples (Drünert et al. 2018). However, due to the complexity of the reduced symmetry, only a few papers have been published on the extinction spectra of spheroidal metal nanoparticles (Porstendorfer et al. 1999; Jain et al. 2006; Liu et al. 2011; Somerville et al. 2016), none of which made any connections to the color effects of the particles. Studying the color effect of copper nanoparticles would require systematic calculations of the extinction spectra over a wide range of different sizes and shapes. This type of research was previously exclusive to professionally trained physicists with a complete comprehension of the electromagnetic theories to write dedicated codes for solving specific problems. Fortunately, thanks to the broad impact of particle optics, many user-friendly algorithm and codes with more general applications have been published in recent years, making the abstract and convoluted mathematical equations accessible to more researchers interested in the subject. Therefore, the puzzling color effect of the Oregon sunstone and other Cu-bearing plagioclase feldspars is revisited in this paper, by comparing the experimental UV-VIS spectra to the calculated ones from Cu particles with various sizes and shapes.

Samples and Methods

SMARTIES (Somerville et al. 2016) is used to calculate the absorption and scattering effect of Cu spheroids in plagioclase. The spatial distributions of the scattered light by spherical Cu particles are calculated using MiePlot (Laven 2003, 2004). A constant refractive index of 1.56 for intermediate plagioclase is used in the calculation. The analytical expression of the Cu dielectric constant by Fitio et al. (2020), based on the most recent experimental data (Babar and Weaver 2015; McPeak et al. 2015), is used in the calculation. It is known that the dielectric constant of nanoparticles may be different from the bulk material due to the average path of free electrons being limited by the particle size (Scaffardi and Tocho 2006; Santillán et al. 2013). However, this effect is only slightly noticeable for Cu particles smaller than 5 nm (Santillán et al.

2013), and does not change the shape of absorption and extinction spectrum, therefore, is not considered for the analysis in this work.

Spheroids are ellipsoids with rotational symmetry (stretched or squished spheres along one axis), which can be defined by two semi-axes, the equatorial radius $\boldsymbol{a}$, and the center-to-pole distance $\boldsymbol{c}$ (along the symmetry axis). Prolate spheroids are elongated along the rotational axis ($\frac{\boldsymbol{c}}{\boldsymbol{a}} > 1$), whereas oblate spheroids are contracted ($\frac{\boldsymbol{c}}{\boldsymbol{a}} < 1$). Spheroids are reduced to spheres when the center-to-pole distance is equal to the equatorial radius ($\frac{\boldsymbol{c}}{\boldsymbol{a}} = 1$). Laboratory coordinates (x y z) are defined with the Z-axis along the rotational axis of the spheroids, and the X- and Y-axes inside the equatorial plane (Figure 2). The absorption and scattering spectra of three different incident light orientations are calculated for each particle size and shape: $K_ZE_XM_Y$ (incident along Z-axis with the electric field linearly polarized along X-axis, marked by the blue arrow in Figure 2), $K_XE_YM_Z$ (red arrow), and $K_YE_ZM_X$ (green arrow). Due to the rotational symmetry of the spheroid, all directions in the XY plane are equivalent. Therefore, these three orientations represent all the possible incident light along the principal axes of the spheroid, which can be labeled with respect only to the Z axis unambiguously as K_z, M_z and E_z (propagation direction, magnetic field polarization, and electric field polarization along the Z-axis respectively).

In most previous works (Porstendorfer et al. 1999; Somerville et al. 2016), the extinction spectra of spheroidal particles with different shapes ($\frac{\boldsymbol{c}}{\boldsymbol{a}}$ ratios) are compared to each other with a fixed volume or surface area. However, the calculation in this work shows that the optical effect of the Cu spheroid is more dependent on the equatorial radius than the volume or surface area of the particle. Therefore, the absorption and scattering spectra are calculated for Cu spheroids with the equatorial radius $\boldsymbol{a}$ ranging from 1 nm to 100 nm (1 nm interval), and aspect ratio $\frac{\boldsymbol{c}}{\boldsymbol{a}}$ from 0.5 to 2 (0.05 interval) for each particular radius $\boldsymbol{a}$. The spectrum for each radius and aspect ratio is calculated for wavelengths between 300 nm and 1000 nm (5 nm interval). The plots presented in this paper are interpolated from the calculated results to produce smooth spectra.

To compare the computational results with experimental data, five samples are selected for spectroscopic analysis in this paper, including one Cu-free labradorite (DD-012) from the Dust Devil Mine, one strongly pleochroic labradorite sunstone (SB-001) from the Sunstone Butte Mine, and three pleochroic Cu-bearing andesine from China (A110, A112, and A090). All the

142 samples are cut into wafers (2-4 mm thick) along the most pleochroic direction, with the two
143 parallel surfaces polished. The extinction spectra of the samples are collected on a PerkinElmer
144 Lambda 950 UV/VIS Spectrometer. The chemical compositions of the samples are analyzed
145 with Laser Ablation Inductively Coupled Plasma Mass Spectrometry (LA-ICP-MS), using a
146 Thermo Scientific iCAP Qc ICP-MS connected to an Elemental Scientific Lasers NWR213 laser
147 ablation system (frequency quintupled Nd:YAG laser operated in Q-switched mode at a
148 wavelength of 213 nm and pulse duration of 4 ns). Standard GSD-1G, GSE-1G and NIST SRM
149 610 were used for external calibration. A 100μm-diameter laser spot size was used to ablate the
150 sample at a 20 Hz repetition rate with a fluence (energy density) of ~6 J/cm^2. The compositions
151 of two spots are analyzed for each sample, one on the edge (colorless) and one in the center. No
152 obvious chemical zoning of major or trace element is detected in any of the samples. The major
153 feldspar element concentrations (Ca, Na, K, Al and Si) of the samples are normalized to 4
154 (Al+Si) per formula and listed in Table 1. The concentrations of selected trace elements are listed
155 in Table 2.

156 The natural Oregon sunstones show a wide variety of colors, including several different green
157 and blue hues (oregonsunstoneguide.com/types-and-colors.html). Unfortunately, it is not
158 possible to include more than one natural green sunstone sample in this study due to the extreme
159 rarity and value of these colors. The Cu-bearing andesine (A110, A112, and A090) from China
160 are artificially diffused, indicated by the high Cu concentrations (> 500 ppmw) and colorless
161 rims near the surfaces and twin boundaries of the crystals (McClure 2009). These Cu-diffused
162 samples are included in this study for comparison with the natural stone, and to demonstrate the
163 wide range of spectra that can be produced by the Cu particles.

164

165 **Computational Results**

166 The extinction (wavelength dependent) of a single particle is measured by the extinction cross-
167 section (C_{ext}), which is the sum of absorption cross-section (C_{abs}) and total scattering cross-
168 section (C_{sca}) expressed in units of area. Because extinction generally increases with the size of a
169 scattering particle, extinction efficiency (Q_{ext}), defined as the ratio between the extinction cross-
170 section and the geometrical cross-sectional area (projected area to be accurate), is commonly
171 used to quantify the effectiveness of light extinction by a particle. However, the geometrical

This is the peer-reviewed, final accepted version for American Mineralogist, published by the Mineralogical Society of America.
The published version is subject to change. Cite as Authors (Year) Title. American Mineralogist, in press.
DOI: https://doi.org/10.2138/am-2022-8325. http://www.minsocam.org/

cross section is not very meaningful when the collective effect of multiple particles is concerned, especially when the particles are not spherical. Therefore, we define extinction power (X_{ext}) (along with absorption and scattering power, X_{abs} and X_{sca}) to be the ratio between the extinction cross-section and the volume of the particle:

$$X_{ext} = X_{abs} + X_{sca} = \frac{C_{abs} + C_{sca}}{V} = \frac{C_{ext}}{V}$$

Assuming no interaction between the scattered light from different Cu particles in the feldspar (no multiple scattering), the total extinction would be the sum of the extinctions from all the individual particles:

$$C_{ext} = \sum_{i=1}^{N} (C_{ext})_i = \sum_{i=1}^{N} (X_{ext})_i V_i = \langle X_{ext} \rangle V_{Cu}$$

$$= \langle X_{ext} \rangle \frac{V_{Cu}}{V_{fs}} V_{fs} = \langle X_{ext} \rangle \frac{m_{Cu}}{m_{fs}} \frac{\rho_{fs}}{\rho_{Cu}} V_{fs} = \frac{\rho_{fs}}{\rho_{Cu}} \langle X_{ext} \rangle w_{Cu} V_{fs}$$

, where w_{Cu} is the mass fraction of the Cu particles in the feldspar, and $\langle X_{ext} \rangle$ is the average extinction power of all the Cu particles. The incident light through a Cu-sunstone is therefore attenuated following the equation:

$$-\frac{dI}{I} = \frac{dC_{ext}}{C_{fs}} = \frac{\rho_{fs}}{\rho_{Cu}} \langle X_{ext} \rangle w_{Cu} \frac{dV_{fs}}{C_{fs}} = \frac{\rho_{fs}}{\rho_{Cu}} \langle X_{ext} \rangle w_{Cu} d\boldsymbol{t}$$

, in which C_{fs} and $\boldsymbol{t}$ are the geometrical cross-sectional area and the thickness of the feldspar crystal respectively. Therefore, the transmitted intensity can be described by equation (Beer–Lambert law):

$$I_{tra}(\boldsymbol{t}) = I_0 e^{\frac{-\rho_{fs}}{\rho_{Cu}} \langle X_{ext} \rangle w_{Cu} \boldsymbol{t}} = I_0 10^{\frac{-\rho_{fs}}{\rho_{Cu} \ln 10} \langle X_{ext} \rangle w_{Cu} \boldsymbol{t}} = I_0 10^{-0.131 \langle X_{ext} \rangle w_{Cu} \boldsymbol{t}}$$

, which means the average extinction power $\langle X_{ext} \rangle$ multiplied by a constant ($\frac{\rho_{fs}}{\rho_{Cu} \ln 10} = 0.131$) is the mass attenuation (extinction) coefficient of the Cu particles, which is an intensive property only dependent on their shapes and sizes.

The radius vs wavelength maps for the absorption, scattering and extinction power (X_{abs}, X_{sca}, and X_{ext}) of spherical Cu particles are shown in Figure 3. Note that the color maps are plotted in the log scale for easy comparison. The same maps plotted in linear color scale can be found in Figure S1 in Supplementary Material for better contrast within each map. The absorption mainly

192 occurs for particles of radius less than ~40 nm at wavelengths below 600 nm, peaking at ~560
193 nm caused by the localized surface plasmon resonance (LSPR) (Petryayeva and Krull 2011). The
194 absorption power drops dramatically for spheres larger than 40 nm in radius. The scattering
195 power of the Cu spheres, on the other hand, is negligible for radius less than 20 nm. The
196 scattering mainly occurs at wavelengths over 550 nm, with the scattering peak moving towards
197 longer wavelength with larger particles. The total extinction power, therefore, is dominated by
198 absorption for smaller particles (R < 35 nm) and scattering for larger particles (R > 35 nm). A
199 second scattering peak can be observed for particles with radius larger than 70 nm. The
200 absorption, scattering and extinction maps of spherical Cu particles in labradorite are very
201 similar to Cu particles in glass as calculated by Drünert et al. (2018), which is expected given the
202 similar refractive indices between feldspar and glass.

203 To illustrate how the spheroidal shape changes the optical effect of the Cu particles, the
204 absorption, scattering and extinction power maps of three incident light orientations are plotted
205 against wavelength and aspect ratio $\frac{\boldsymbol{c}}{\boldsymbol{a}}$ for Cu spheroids with $\boldsymbol{a}$ = 35 nm in Figure 4. The maps of
206 incident light along the Z-axis (K_Z, blue arrow in Figure 2) is almost identical to the maps of
207 incident light with the polarization plane perpendicular to the Z-axis (M_Z, red arrow in Figure 2).
208 The peak position in the K_Z and M_Z maps does not change with the aspect ratio for prolate
209 spheroids ($\frac{\boldsymbol{c}}{\boldsymbol{a}} > 1$), and only slightly shifts towards longer wavelength for oblate spheroids ($\frac{\boldsymbol{c}}{\boldsymbol{a}} <$
210 1). On the other hand, the aspect ratio has a very dramatic effect on the extinction spectrum of
211 the incident light with E_Z polarization. The extinction peak shifts quickly towards the longer
212 wavelength with increasing $\frac{\boldsymbol{c}}{\boldsymbol{a}}$ ratio in the E_Z map, getting broader and stronger at the same time.
213 The scattering power of the spheroid decrease for K_Z and M_Z but increase for E_Z with increasing
214 $\frac{\boldsymbol{c}}{\boldsymbol{a}}$ ratio, indicating that the spheroid scatters light more effectively when the polarization is
215 aligned with its longer dimension. The Cu spheroids with other sizes behaves similarly, except
216 the E_Z scattering peaks shifts and broadens towards the longer wavelengths with increasing $\frac{\boldsymbol{c}}{\boldsymbol{a}}$
217 ratio even faster for larger spheroids (a movie showing continuously changing maps from $\boldsymbol{a}$ = 0
218 nm to $\boldsymbol{a}$ = 100 nm can be found in VIDEO-1 in Supplementary Material).

219 The size vs wavelength maps for the absorption, scattering and extinction power of Cu particles
220 with fixed $\frac{\boldsymbol{c}}{\boldsymbol{a}}$ ratios of 0.5 and 2 are plotted in Figure 5 and Figure 6. Similar to Figure 4, the K_Z

maps are almost the same as the M_Z maps for both prolate and oblate spheroids. The only noticeable differences are that the M_Z maps show an extra peak for the oblate spheroids ($\boldsymbol{a} > 40$ nm, marked with dotted ellipsoid in Figure 5), whereas the K_Z maps have an additional peak for the prolate spheroids (40 nm < $\boldsymbol{a}$ < 80 nm, Figure 6). These maps show more clearly how the extinction power dramatically changes with different polarization. Both the absorption and scattering power are more than 20 times stronger when the polarization of the incident light is parallel to the longer dimension of the spheroid than perpendicular to it. Similar to the spherical particles (Figure 3), absorption is the main effect for small particles and scattering quickly takes over at around $\boldsymbol{a}$ = 35 nm with increasing particle size. The E_Z maps have similar shapes as the other orientations, except extended or contracted by a factor of $\frac{\boldsymbol{c}}{\boldsymbol{a}}$. In prolate spheroids (Figure 6), the LSPR peak in the E_Z map, which is completely separated from the absorption band at shorter wavelengths ($\lambda < 570$ nm), is much stronger than in spheres (Figure 3) or oblate spheroids (Figure 5), and strongly shifted towards longer wavelengths ($\lambda > 620$ nm). A movie showing the maps continuously transforming from Figure 5 to Figure 6 with increasing $\frac{\boldsymbol{c}}{\boldsymbol{a}}$ can be found in VIDEO-2 of Supplementary Material.

Unlike absorption, the scattered energy by Cu particles is not immediately lost (transferred to heat) and may affect the observed color in ways other than simple extinction. Therefore, it is worth considering the spatial distribution of the scattered light. The phase functions $F(\theta, \varphi)$ (normalized scattered intensity as a function of polar angle θ and azimuthal angle φ of the scattered direction) of spherical particles of radius 60 nm, 80 nm and 100 nm at $\lambda = 600$ nm are plotted in Figure 7. Scattering of Cu sphere with radius of 60 nm or smaller can be approximately described by Rayleigh scattering, in which the scattered intensity is constant in the plane perpendicular to the polarization direction, and proportional to $\cos^2\theta$ within the polarization plane. As the Cu sphere gets larger, the scattered light shifts towards the forward direction ($\theta < 90°$). At R = 100 nm, ~35% of the light is scattered in the backward direction (Figure 7). Nonetheless, the energy of incident light from one direction is spread in different directions in 3D space, which means the extinction power in Figure 3-6 is a good measurement of the extinction of light in the forward direction ($\theta = 0°$). The phase functions of spheroidal particles are very similar to spherical particles as shown by previous studies (Asano and Yamamoto 1975; Asano 1979; Mishchenko et al. 2000, 2002a; Mishchenko and Travis 2003). It

is known that for given refractive indices of the particle and the matrix, the phase function, which is dimensionless, is only dependent on the ratio between the particle diameter and the wavelength (scale invariance rule) (Mishchenko et al. 2002b). This means for a fixed particle size, light with shorter wavelengths would be more preferably scattered in the forward direction relative to light with longer wavelengths. However, this effect is negligible compared to the difference in the total scattering power at different wavelengths (Figure 3), and cannot affect the observed color of Cu-sunstone.

Only the optical effects of the Cu particles inside plagioclase crystals have been considered so far. The feldspar crystals themselves are often light yellow colored from Fe^{3+} substitution in the framework (Hofmeister and Rossman 1983), which also contribute to the appearance of the Cu-sunstones. The extinction (attenuation) of a Cu-sunstone can be calculated by simply adding the absorbance of the feldspar to the attenuance of the Cu particles:

$$\mathrm{A_{sun}} = \mathrm{A_{Cu}} + \mathrm{A_{fs}}$$

, in which $\mathrm{A_{Cu}} = 0.131\langle \mathrm{X_{ext}} \rangle w_{\mathrm{Cu}}$. An example of the calculated extinction spectrum of a Cu-sunstone containing 10 ppmw of spherical Cu particles with 5 nm radius is shown in Figure 8. The resulting spectrum is almost identical to the experimental data reported by (Hofmeister and Rossman 1983, 1985; Susawee 2013; Susawee and Sutthirat 2014), and very similar to the absorption spectrum of the copper ruby glass studied by (Durán et al. 1984; Doremus et al. 1992; Akai et al. 1993; Nakai et al. 1999; Capatina 2005; Macalik 2005).

From the calculated spectrum, the observed colors (RGB values) of the Cu-sunstones can be calculated following the method by Sun et al. (2017). To best compare the color effect of Cu particles with different sizes and shapes, the computed colors are mapped against equatorial radius ($\boldsymbol{a}$) and aspect ratio ($\frac{\boldsymbol{c}}{\boldsymbol{a}}$) for 3mm thick Cu-sunstones containing ~20 ppmw of Cu particles in Figure 9. These parameters are selected to produce the most saturated colors overall. Only incident light perpendicular to the rotational axis ($\mathrm{M_Z}$ and $\mathrm{E_Z}$) is calculated, because this is the direction with the strongest potential pleochroism, and the $\mathrm{K_Z}$ map would be identical to the $\mathrm{M_Z}$ map given the similarity in the extinction power maps (Figure 4-6). The color map with unpolarized incident light is also calculated by averaging the extinction spectrum of the two polarization following the equation (Libowitzky and Rossman 1996):

This is the peer-reviewed, final accepted version for American Mineralogist, published by the Mineralogical Society of America.
The published version is subject to change. Cite as Authors (Year) Title. American Mineralogist, in press.
DOI: https://doi.org/10.2138/am-2022-8325. http://www.minsocam.org/

$$A_{unpol} = -\log\left(\frac{10^{-A_Y} + 10^{-A_Z}}{2}\right)$$

A region of intense red color is resulted for particles with radius less than 35 nm in the M_Z color map. The color quickly transitions to deep green as the radius passes ~40 nm. The color gets washed out with larger particle sizes. The E_Z color map show very similar colors, but with significantly different shapes for each region. The region of the red color extends to larger particle sizes for oblate spheroids, which contracts and disappears with increasing aspect ratio. The strongest pleochroism appears with Cu particles of ***a*** ~30 nm and ***c*** ~40 nm, showing deep red and green color with light polarized perpendicular and parallel to the Z-axis respectively. Oblate particles with ***a*** ~45 nm and ***c*** ~30 nm show similar pleochroism, but with lighter orange color for E_Z incident light. Spheroids (oblate or prolate) of smaller sizes are also slightly pleochroic, with the red color more saturated when the incident light is polarized along the longer dimensions of the spheroids. The red region in the unpolarized color map is the intersection of the red regions in both the M_Z and E_Z color maps, bounded by a strip of green region. The red color in the unpolarized color map is more homogeneous and does not change with different particle sizes or shapes. It should be noted that thicker crystals with less Cu-particle concentration may produce colors of similar saturation, but with slightly different hues.

Comparison to experimental data and discussion

Only metallic Cu particles are considered in this paper, as no other form of Cu-containing precipitates has been reported in feldspars, and Cu oxide particles have been shown to have completely different optical effects (Drünert et al. 2018). The optical effects of Cu particles in plagioclase feldspars are modeled with spheroids, because they are the simplest (most symmetrical) shapes possible that can create pleochroism. It is also not a bad assumption for the real Cu-sunstone, since the shapes of metallic nanoparticles are mostly controlled by minimizing its surficial or interfacial energy. Spherical shape is expected for particles in isotropic matrix such as liquid or glass, and the anisotropy of a crystal with low symmetry (such as plagioclase) may distort them into spheroids or ellipsoids. Spherical and spheroidal nanoparticles of coinage metal are often directly observed in glass or solution using transmission electron microscope (TEM) (Doremus and Turkalo 1976; Barber and Freestone 1990; Doremus et al. 1992; Link and

El-Sayed 1999; Kaempfe et al. 2001; Suszyńska et al. 2003, 2010; Gil et al. 2005; Macalik 2005; Bring 2006; Amendola and Meneghetti 2009; Choi et al. 2012; Pellerin et al. 2013; Boita et al. 2017). Small Cu particles (⌀ < 20 nm) in plagioclase showing almost perfect spheroidal shapes have been directly observed in TEM recently (Wang et al. 2019). The larger Cu particles (⌀ ~100 nm) in natural pleochroic Oregon sunstones reported by Xu et al. (2017) show less regular shapes, and are accompanied by nano-precipitates of protoenstatite, suggesting a more complicated exsolution process of Cu in natural plagioclase. Research on Cu precipitates in plagioclase is quite limited, mostly due to their extremely low concentration, requiring tens or even hundreds of hours on a TEM to locate and image only a handful of Cu particles. The diffusion and exsolution mechanism of Cu in feldspars is also poorly understood. Nonetheless, based on the limited observations, spheroid is a reasonable approximation for the size range calculated in this work. Particles with larger sizes, on the other hand, are expected to deviate significantly from ideal spheroidal shapes, and approach thin flakes as they grow large enough to be visible with optical microscope.

For comparison with the computational results, the polarized extinction spectra of the four Cu-sunstone samples are measured along the maximum (dotted line) and minimum (solid line) extinction direction (Figure 10). Images showing the sample colors under polarized transmission light corresponding to the extinction spectra are also shown with the plots. The orientation of an absorber in a triclinic crystal is not constrained by symmetry, thus independent from the orientation of the optical indicatrix (Dowty 1978; Libowitzky and Rossman 1996). The orientation effect of multiple Cu particles is even more complicated, considering the extinction power is not only dependent on the polarization, but also the incidence direction (Figure 5, 6). Measuring the average orientation of the Cu particles relative to the feldspar crystal is beyond the scope of this study, therefore the samples are only cut and polished in one orientation. The extinction spectra show a wide variety among the natural and Cu-diffused samples, resulting in different hues of green and red colors. The spectra corresponding to the red colors (minimum extinction in Figure 10*a*, *b*) are the same as previously reported ones (Hofmeister and Rossman 1983, 1985; Rossman 2011). The LSPR peak at ~570nm is slightly broader relative to the spectrum calculated for spherical particles (Figure 8), most likely due to a dispersed distribution of particle sizes and shapes. The green-colored spectra show extinction peaks much stronger than the red ones, occurring anywhere between 590nm and 700nm. The peaks at longer wavelengths

This is the peer-reviewed, final accepted version for American Mineralogist, published by the Mineralogical Society of America.
The published version is subject to change. Cite as Authors (Year) Title. American Mineralogist, in press.
DOI: https://doi.org/10.2138/am-2022-8325. http://www.minsocam.org/

are much broader than the ones at shorter wavelengths, agreeing with the calculated extinction spectra (Figure 3-6). Note that the extinction peak in the green spectrum of sample SB-001 appears at ~610nm (instead of 630nm), and is much sharper than the previously reported spectra (Hofmeister and Rossman 1983, 1985; Rossman 2011). The large variations in the peak shapes and positions cannot be explained by any absorption from trace elements or intervalence charge transfers. More diverse extinction spectra are certainly expected when more natural Cu-sunstones are studied, considering the wide range of reported colors.

Zoomed images of sample A110 (Figure 10*b*) are shown in Figure 11 with different polarized illuminations. The crystal has a colorless rim of ~0.5 mm wide (typical for treated stones), followed by a 0.2mm red zone (not pleochroic), and then transfers inward to a strongly pleochroic region (green-red). It should be noted that even though the polarization of the maximum extinction (dark green color) aligns with the twin planes in the feldspar crystal, it cannot be directly used to infer the orientations of the Cu-particles. Because the light inside the sunstone is polarized following the optical indicatrix of the birefringent feldspar, which is independent from the polarization of the incident light (Libowitzky and Rossman 1996). The red zone barely scatter any light under reflective lighting, whereas the pleochroic region scatters light more expressively (Tyndall effect). The backscattered light is also strongly polarized, with much stronger scattering corresponding to the maximum extinction (green color under transmission light). This confirms the computational result, where the red color is created by strong absorption of blue and green light ($\lambda < 600$ nm), and the green color by scattering dominated extinction (red and orange light with $\lambda > 570$ nm being scattered away). Images of sample SB-001 under the same polarized illumination are provided in Figure S2 in Supplementary Material, showing the colors in natural Cu-sunstone are created by the same mechanism as treated stones. The red Tyndall effect in sample SB-001 is better shown in Figure S3.

Under unpolarized transmission light, sample A110 appears similar to Figure 11*b*, except with slightly lighter green color, agreeing with the color map of unpolarized light in Figure 9. However, when observed with ambient illumination and no light source directly behind the crystal, sample A110 appears mostly red, suggesting that the scattered red light also contributes to the observed color. Because light scattered by a particle at depth $\boldsymbol{t}$ from the surface is

This is the peer-reviewed, final accepted version for American Mineralogist, published by the Mineralogical Society of America.
The published version is subject to change. Cite as Authors (Year) Title. American Mineralogist, in press.
DOI: https://doi.org/10.2138/am-2022-8325. http://www.minsocam.org/

attenuated by a factor of $10^{-2(A_{Cu}+A_{fs})t}$ for the round trip from the surface, the scattered intensity by all the particles at depth $\boldsymbol{t}$ inside a crystal can be described by equation:

$$\frac{dI_{bsc}}{I_0} = 10^{-2(A_{Cu}+A_{fs})t}\frac{\rho_{fs}}{\rho_{Cu}}\langle X_{bsc}\rangle w_{Cu}\, dt$$

, in which $\langle X_{bsc}\rangle$ is the average backscattering power of the particles (generally proportional to the total scattering power $\langle X_{sca}\rangle$). Therefore, the total backscattered intensity by a crystal with total thickness of $\boldsymbol{t}$ can be described by equation:

$$I_{bsc}(t) = \frac{B_{Cu}I_0}{2(A_{Cu}+A_{fs})}\left(1 - 10^{-2(A_{Cu}+A_{fs})t}\right) = \frac{B_{Cu}}{2(A_{Cu}+A_{fs})}(I_0 - I_{tra}(2t))$$

, where $B_{Cu} = 0.131\langle X_{bsc}\rangle w_{Cu}$, which is the backscattering coefficient of the Cu particles. With increasing thickness, the backscattered intensity approaches the maximum value of $\frac{B_{Cu}I_0}{2(A_{Cu}+A_{fs})}$ twice as fast as the transmitted intensity approaches 0. This means the color of the same Cu-sunstone crystal may change from red (from the scattered light) to green (from the transmitted light) when it is cut thin enough. Note that the ratio $\frac{B_{Cu}}{2(A_{Cu}+A_{fs})}$ approaches 0 with low Cu concentration (or small particle sizes), and converges to a constant of $\frac{B_{Cu}}{2A_{Cu}}$ for high Cu concentration. This the reason why the best green colors are only found in larger crystals with low particle concentrations (sample SB-001 as shown in Figure S3), because the scattered light intensity is negligible and does not affect the color under most lighting conditions.

As shown in Figure 9, the colors created by extinction become more and more washed out (whitened) as the extinction power decreases with increasing particles sizes. This explains the scarcity of the green colors in natural Cu-sunstones, as such colors can only be created by Cu particles within a very narrow range of sizes. As the particle size increases, the enhancement of surface electric field, which is responsible for the strong scattering power for the small Cu particles, drops dramatically due to the decreasing surface curvature. This means scattering from the larger Cu particles is mostly surface reflection, which should be similar to bulk metallic Cu. For example, the scattered intensity by a Cu sphere with a radius of 2μm is plotted against wavelength and scattering angle in Figure 12. Around 50% of the scattered energy are uniformly diffracted within the cone of $\theta < 5°$ in the forward direction. For all the scattering angles larger than 30°, the scattered energy shows a sharp increase around 560 nm very similar to the

393 reflectivity of bulk metallic Cu, with the longer wavelengths scattered about twice as much as the
394 shorter wavelengths. Note that the aforementioned features are not exclusive to the spherical
395 particles, only the ripples in the scattered intensity map is characteristic to the shape, which
396 eventually disappear with increasing size. In fact, the extinction cross section of a large Cu
397 particle is no longer wavelength dependent, because light is either blocked (absorption +
398 reflection) or diffracted uniformly. Therefore, the only color that can be observed is the color of
399 the reflected light by the Cu particles, which is almost the same as bulk metallic copper. This is
400 actually the color of the aventurescence or "schiller" effect that the Oregon sunstones are best
401 known for [Figure S1-4 in Xu et al. (2017)]. More total exsolved Cu may be needed for the
402 larger particles to create an observable optical effect, due to the reduced scattering power with
403 increasing particle sizes, even though the surface-to-volume ratio of the larger Cu particles is
404 often compensated by flattened shapes.

405 It is also worth noting that the natural Cu-sunstone from Oregon (SB-001) shows stronger
406 pleochroism than the Cu-diffused samples (Figure 10), suggesting stronger anisotropy and
407 smaller deviation in the particle shapes and orientations. The Cu concentrations in the Cu-
408 diffused samples are much higher (~10×) than the natural Oregon sunstone with similar color
409 saturation (attenuance), indicating that a much smaller fraction of Cu has exsolved as Cu
410 particles in the treated stones. These distinctions reflect different thermal histories between
411 natural and treated Cu-sunstones, and may provide clues on separating untreated stones from Cu-
412 diffused ones in a gemology lab. The labradorite phenocryst may have equilibrated with the Cu-
413 bearing basaltic magma for over 1000 years before eruption (Ramos et al. 2005) and cooling
414 after eruption can take months or even years (Long and Wood 1986; Petcovic and Dufek 2005),
415 which is significantly longer than the time needed to treat the stones in a laboratory (Emmett and
416 Douthit 2009). The protoenstatite precipitates found in natural Oregon sunstones (Xu et al.
417 2017), as well as their complicated structural states (Jin et al. 2018, 2019), could also affect the
418 nucleation of Cu particles. Further study on the diffusion and exsolution of Cu in plagioclase
419 feldspars is required to fully understand the formation process of these Cu particles.

420

421 **Implications**

Metallic Cu particles alone can clearly explain all the color effects that are observed in natural and treated Cu-sunstones, without involving any other chromophores. The Cu nanoparticles creates color with a mechanism different from the other colored gemstones. Smaller particles (⌀ < 80 nm) mainly absorb blue and green light and allow red light to pass through, and slightly larger particles (80 nm < ⌀ < 120 nm) strongly scatter red and orange light away to allow more green light through. Strong pleochroism is created when elongated particles of similar sizes are orientated in the same direction. The red Tyndall effect can be observed in green/pleochroic Cu-sunstones, but only under intense and directional lighting (i.e. fiber optic illuminator). The appearance of the Cu-sunstone is also dependent on the particle concentration and crystal size, which controls the intensity ratio between the scattered light and the transmitted light. Only a small amount (~20 ppmw) of exsolved Cu is needed to produce saturated colors, and the colorless rims of the Cu-sunstones contain similar amount of Cu as the colored cores, indicating that most of the Cu is dissolved in the feldspar lattice (presumably as Cu^{+} or Cu^{2+}) with no detectable absorption effect in the visible light range.

Analyzing the concentration, as well as size and shape distribution of Cu particles in natural and treated Cu-sunstones, is essential in understanding the mechanism of the fast diffusion and exsolution process of Cu in plagioclase crystals. Absorption spectra have been regularly used in determining both the size and shape distribution of small gold and silver nanoparticles in colloidal solutions (Eustis and El-Sayed 2006; Haiss et al. 2007; Amendola and Meneghetti 2009; Kolwas et al. 2009; Resano-Garcia et al. 2015; Battie et al. 2017; Ngumbi et al. 2018; Kumar et al. 2019). The size distribution of larger Cu spheres in glass has also been studied with backscattering spectra (Drünert et al. 2018). The results from this work show that these spectroscopy-based studies are not limited to small particle sizes or spherical shapes. Multiple spectra from one single sample (polarized extinction and backscattering) can also be used for more comprehensive analyses.

The special optical properties of metallic nano-particles have been used to create colors in glasses for centuries, and is still a hot topic in the research of optical materials. The observed colors of Cu-sunstones are not only dependent on the polarization of the incident light, but also the relative direction of the incident light to the observer. The scattering dominated extinction in Cu-sunstone provides new possibilities for designing novel materials with special color effects

and optical properties, if the particle sizes and shapes can be precisely controlled within a narrow range.

Acknowledgement

This research is supported by the Richard T. Liddicoat Postdoctoral Research Associate Fellowship program at GIA. The authors thank Shane F. McClure for providing the natural Oregon sunstone sample, and Philip Laven for patient explanations on the different functions and outputs of the MiePlot program. We thank Anne Hofmeister and George Rossman for many constructive comments, and Associate Editor Simon Redfern for handling the manuscript.

References

Akai, T., Kadono, K., Yamanaka, H., Sakaguchi, T., Miya, M., and Wakabayashi, H. (1993) Preparation of Copper-Ruby Glasses by Sputtering and Their Optical Properties. Journal of the Ceramic Society of Japan, 101, 105–107.

Amendola, V., and Meneghetti, M. (2009) Size Evaluation of Gold Nanoparticles by UV−vis Spectroscopy. The Journal of Physical Chemistry C, 113, 4277–4285.

Anderson, O. (1917) Aventurine labradorite from California. American Mineralogist, 2, 91.

Asano, S. (1979) Light scattering properties of spheroidal particles. Applied optics, 18, 712–723.

Asano, S., and Yamamoto, G. (1975) Light Scattering by a Spheroidal Particle. Applied Optics, 14, 29–49.

Babar, S., and Weaver, J.H. (2015) Optical constants of Cu, Ag, and Au revisited. Applied Optics, 54, 477–481.

Bandiera, M., Lehuédé, P., Verità, M., Alves, L., Biron, I., and Vilarigues, M. (2019) Nanotechnology in Roman Opaque Red Glass from the 2nd Century AD. Archaeometric Investigation in Red Sectilia from the Decoration of the Lucius Verus Villa in Rome. Heritage, 2, 2597–2611.

Barber, D.J., and Freestone, I.C. (1990) An Investigation of the Origin of the Colour of the Lycurgus Cup by Analytical Transmission Electron Microscopy. Archaeometry, 32, 33–45.

Battie, Y., Izquierdo-Lorenzo, I., Resano-Garcia, A., Naciri, A.E., Akil, S., Adam, P.M., and Jradi, S. (2017) Determination of gold nanoparticle shape from absorption spectroscopy and ellipsometry. Applied Surface Science, 421, 301–309.

Boita, J., Nicolao, L., Alves, M.C.M., and Morais, J. (2017) Controlled growth of metallic copper nanoparticles. New Journal of Chemistry, 41, 14478–14485.

Bring, T. (2006) Red Glass Coloration - A Colorimetric and Structural Study. Ph.D., KTH Royal Institute of Technology, Stockholm, Sweden.

Brun, N., Mazerolles, L., and Pernot, M. (1991) Microstructure of opaque red glass containing copper. Journal of Materials Science Letters, 10, 1418–1420.

Capatina, C. (2005) The Study of Copper Ruby Glass. Ceramics Silikaty, 49, 283–286.

Choi, C.S., Jo, Y.H., Kim, M.G., and Lee, H.M. (2012) Control of chemical kinetics for sub-10 nm Cu nanoparticles to fabricate highly conductive ink below 150°C. Nanotechnology, 23, 065601.

Doremus, R., Kao, S.C., and Garcia, R. (1992) Optical absorption of small copper particles and the optical properties of copper. Applied Optics, 31, 5773–5778.

Doremus, R.H. (1964) Optical Properties of Small Gold Particles. The Journal of Chemical Physics, 40, 2389–2396.

Doremus, R.H., and Turkalo, A.M. (1976) Electron microscopy and optical properties of small gold and silver particles in glass. Journal of Materials Science, 11, 903–907.

Dowty, E. (1978) Absorption optics of low-symmetry crystals — Application to titanian clinopyroxene spectra. Physics and Chemistry of Minerals, 3, 173–181.

Drünert, F., Blanz, M., Pollok, K., Pan, Z., Wondraczek, L., and Möncke, D. (2018) Copper-based opaque red glasses – Understanding the colouring mechanism of copper nanoparticles in archaeological glass samples. Optical Materials, 76, 375–381.

Durán, A., Fernández Navarro, J.M., García Solé, J., and Agulló-López, F. (1984) Study of the colouring process in copper ruby glasses by optical and EPR spectroscopy. Journal of Materials Science, 19, 1468–1475.

Emmett, J.L., and Douthit, T.R. (2009) Copper Diffusion in Plagioclase p. 15. GIA News from Research, GIA.

Eustis, S., and El-Sayed, M.A. (2006) Determination of the aspect ratio statistical distribution of gold nanorods in solution from a theoretical fit of the observed inhomogeneously broadened longitudinal plasmon resonance absorption spectrum. Journal of Applied Physics, 100, 044324.

Farfan, G., and Xu, H. (2008) Pleochroism in calcic labradorite from Oregon: Effects from size and orientation of nano- and micro-precipitates of copper and pyroxene. In Geochimica et Cosmochimica Acta Vol. 72, p. A256. Presented at the Goldschmidt, Vancouver, BC, Canada.

Fitio, V., Yaremchuk, I., Vernyhor, O., and Bobitski, Y. (2020) Analytical expressions for spectral dependences of silver, gold, copper and aluminum dielectric permittivity. Optica Applicata, 50, 171–184.

Freestone, I. (1987) Composition and microstructure of early opaque red glass. Early Vitreous Materials, 173–191.

Freestone, I., Meeks, N., Sax, M., and Higgitt, C. (2007) The Lycurgus Cup — A Roman nanotechnology. Gold Bulletin, 40, 270–277.

Gans, R. (1912) Über die Form ultramikroskopischer Goldteilchen. Annalen der Physik, 342, 881–900.

——— (1915) Über die Form ultramikroskopischer Silberteilchen. Annalen der Physik, 352, 270–284.

Gil, C., Villegas, M.A., and Fernandez Navarro, J.M. (2005) Preparation and study of superficially coloured lead glass. Journal of Materials Science, 40, 6201–6206.

Haiss, W., Thanh, N.T.K., Aveyard, J., and Fernig, D.G. (2007) Determination of Size and Concentration of Gold Nanoparticles from UV−Vis Spectra. Analytical Chemistry, 79, 4215–4221.

Hofmeister, A.M., and Rossman, G.R. (1983) COLOR in FELDSPARS. In P.H. Ribbe, Ed., Feldspar Mineralogy pp. 271–280. Mineralogical Society of American, Washington, D.C.

——— (1984) Determination of Fe^{3+} and Fe^{2+} concentrations in feldspar by optical-absorption and electron-paramagnetic-res spectroscopy. Physics and Chemistry of Minerals, 11, 213–224.

——— (1985) Exsolution of metallic copper from Lake County labradorite. Geology, 13, 644–647.

Hutter, E., and Fendler, J.H. (2004) Exploitation of Localized Surface Plasmon Resonance. Advanced Materials, 16, 1685–1706.

Jain, P.K., Lee, K.S., El-sayed, I.H., and El-sayed, M.A. (2006) Calculated absorption and scattering properties of gold nanoparticles of different size, shape, and composition: applications in biological imaging and biomedicine. J. Phys. Chem. B, 7238–7248.

Jin, S., Wang, X., and Xu, H. (2018) Revisiting the $I\bar{1}$ structures of high-temperature Ca-rich plagioclase feldspar — a single-crystal neutron and X-ray diffraction study. Acta Crystallographica Section B, 74, 152–164.

Jin, S., Xu, H., Wang, X., Zhang, D., Jacobs, R., and Morgan, D. (2019) The incommensurately modulated structures of volcanic plagioclase: displacement, ordering and phase transition. Acta Crystallographica Section B, 75, 643–656.

Kaempfe, M., Seifert, G., Berg, K.-J., Hofmeister, H., and Graener, H. (2001) Polarization dependence of the permanent deformation of silver nanoparticles in glass by ultrashort laser pulses. The European Physical Journal D, 16, 237–240.

Kalenskii, A.V., Zvekov, A.A., Nikitin, A.P., and Anan'eva, M.V. (2015) Optical Properties of Copper Nanoparticles. Russian Physics Journal, 58, 1098–1104.

Kolwas, K., Derkachova, A., and Shopa, M. (2009) Size characteristics of surface plasmons and their manifestation in scattering properties of metal particles. Journal of Quantitative Spectroscopy and Radiative Transfer, 110, 1490–1501.

Kumar, R., Binetti, L., Nguyen, T.H., Alwis, L.S.M., Agrawal, A., Sun, T., and Grattan, K.T.V. (2019) Determination of the Aspect-ratio Distribution of Gold Nanorods in a Colloidal Solution using UV-visible absorption spectroscopy. Scientific Reports, 9, 17469.

562 Laven, P. (2003) Simulation of rainbows, coronas, and glories by use of Mie theory. Applied
563 Optics, 42, 436–444.

564 ——— (2004) Simulation of rainbows, coronas and glories using Mie theory and the Debye
565 series. Journal of Quantitative Spectroscopy and Radiative Transfer, 89, 257–269.

566 Libowitzky, E., and Rossman, G.R. (1996) Principles of quantitative absorbance measurements
567 in anisotropic crystals. Physics and Chemistry of Minerals, 23, 319–327.

568 Link, S., and El-Sayed, M.A. (1999) Spectral Properties and Relaxation Dynamics of Surface
569 Plasmon Electronic Oscillations in Gold and Silver Nanodots and Nanorods. The Journal
570 of Physical Chemistry B, 103, 8410–8426.

571 Liu, P., Liu, Juan, Liu, Jing, Zhao, X., Xie, J., and Wang, Y. (2011) Scattering properties of an
572 individual metallic nano-spheroid by the incident polarized light wave. Optics
573 Communications, 284, 1076–1081.

574 Long, P.E., and Wood, B.J. (1986) Structures, textures, and cooling histories of Columbia River
575 basalt flows. GSA Bulletin, 97, 1144–1155.

576 Macalik, B. (2005) Optical properties of copper nanoparticles in soda-lime silicate glasses.
577 physica status solidi (c), 2, 608–611.

578 McClure, S.F. (2009) Observations on Identification of Treated Feldspar p. 12. GIA News from
579 Research, GIA, Carlsbad, CA, USA.

580 McPeak, K.M., Jayanti, S.V., Kress, S.J.P., Meyer, S., Iotti, S., Rossinelli, A., and Norris, D.J.
581 (2015) Plasmonic Films Can Easily Be Better: Rules and Recipes. ACS Photonics, 2,
582 326–333.

583 Mie, G. (1908) Beiträge zur Optik trüber Medien, speziell kolloidaler Metallösungen. Annalen
584 der Physik, 330, 377–445.

585 Mishchenko, M.I., and Travis, L.D. (2003) Electromagnetic scattering by nonspherical particles.
586 In Exploring the Atmosphere by Remote Sensing Techniques pp. 77–127. Springer,
587 Berlin, Heidelberg.

588 Mishchenko, M.I., Hovenier, J.W., and Travis, L.D., Eds. (2000) Light Scattering by
589 Nonspherical Particles: Theory, Measurements, and Applications, 721 p. IOP Publishing.

590 Mishchenko, M.I., Travis, L.D., and Lacis, A.A. (2002a) Scattering and absorption properties of
591 nonspherical particles. In Scattering, Absorption, and Emission of Light by Small
592 Particles pp. 279–359. Cambridge University Press/NASA, Cambridge, United Kingdom.

593 ——— (2002b) T-matrix method and Lorenz-Mie theory. In Scattering, Absorption, and
594 Emission of Light by Small Particles pp. 115–190. Cambridge University Press/NASA,
595 Cambridge, United Kingdom.

596 Nakai, I., Numako, C., Hosono, H., and Yamasaki, K. (1999) Origin of the Red Color of
597 Satsuma Copper-Ruby Glass as Determined by EXAFS and Optical Absorption
598 Spectroscopy. Journal of the American Ceramic Society, 82, 689–695.

599 Ngumbi, P.K., Mugo, S.W., and Ngaruiya, J.M. (2018) Determination of Gold Nanoparticles
600 Sizes via Surface Plasmon Resonance. IOSR Journal of Applied Chemistry, 11, 25–29.

601 Papavassiliou, G.C. (1979) Optical properties of small inorganic and organic metal particles.
602 Progress in Solid State Chemistry, 12, 185–271.

603 Parsons, J., Burrows, C.P., Sambles, J.R., and Barnes, W.L. (2010) A comparison of techniques
604 used to simulate the scattering of electromagnetic radiation by metallic nanostructures.
605 Journal of Modern Optics, 57, 356–365.

606 Pellerin, N., Blondeau, J.-P., Noui, S., Allix, M., Ory, S., Veron, O., De Sousa Meneses, D., and
607 Massiot, D. (2013) Control of selective silicate glass coloration by gold metallic
608 nanoparticles: structural investigation, growth mechanisms, and plasmon resonance
609 modelization. Gold Bulletin, 46, 243–255.

610 Petcovic, H.L., and Dufek, J.D. (2005) Modeling magma flow and cooling in dikes: Implications
611 for emplacement of Columbia River flood basalts. Journal of Geophysical Research:
612 Solid Earth, 110, B10201.

613 Petryayeva, E., and Krull, U.J. (2011) Localized surface plasmon resonance: Nanostructures,
614 bioassays and biosensing — A review. Analytica Chimica Acta, 706, 8–24.

615 Porstendorfer, J., Berg, K.-J., and Berg, G. (1999) Calculation of extinction and scattering
616 spectra of large spheroidal gold particles embedded in a glass matrix. Journal of
617 Quantitative Spectroscopy and Radiative Transfer, 63, 479–486.

618 Ramos, F.C., Wolff, J.A., and Tollstrup, D.L. (2005) Sr isotope disequilibrium in Columbia
619 River flood basalts: Evidence for rapid shallow-level open-system processes. Geology,
620 33, 457–460.

621 Resano-Garcia, A., Battie, Y., Naciri, A.E., Akil, S., and Chaoui, N. (2015) Experimental and
622 theoretical determination of the plasmonic responses and shape distribution of colloidal
623 metallic nanoparticles. The Journal of Chemical Physics, 142, 134108.

624 Rossman, G.R. (2011) The Chinese Red Feldspar Controversy: Chronology of Research Through
625 July 2009. Gems & Gemology, 47, 16-30.

626 Ruivo, A., Gomes, C., Lima, A., Botelho, M.L., Melo, R., Belchior, A., and Pires de Matos, A.
627 (2008) Gold nanoparticles in ancient and contemporary ruby glass. Journal of Cultural
628 Heritage, 9, e134–e137.

629 Ruppin, R. (1986) Optical absorption of copper colloids in photochromic glasses. Journal of
630 Applied Physics, 59, 1355–1359.

631 Santillán, J.M.J., Videla, F.A., Scaffardi, L.B., and Schinca, D.C. (2013) Plasmon Spectroscopy
632 for Subnanometric Copper Particles: Dielectric Function and Core–Shell Sizing.
633 Plasmonics, 8, 341–348.

634 Scaffardi, L.B., and Tocho, J.O. (2006) Size dependence of refractive index of gold
635 nanoparticles. Nanotechnology, 17, 1309–1315.

636 Somerville, W.R.C., Auguié, B., and Le Ru, E.C. (2016) SMARTIES: User-friendly codes for
637 fast and accurate calculations of light scattering by spheroids. Journal of Quantitative
638 Spectroscopy and Radiative Transfer, 174, 39–55.

639 Sun, Z., Palke, A.C., Muyal, J., and Mcmurtry, R. (2017) How to facet gem-quality chrysoberyl:
640 Clues from the relationship between color and pleochroism, with spectroscopic analysis
641 and colorimetric parameters. American Mineralogist, 102, 1747–1758.

642 Susawee, N. (2013) Cause of Red Coloring in Gem Plagioclase Feldspar. Masters Thesis,
643 Chulalongkorn University, Bangkok, Thailand.

644 Susawee, N., and Sutthirat, C. (2014) Identification of Natural and Treated Red Feldspar.
645 Bulletin of Earth Sciences of Thailand, 6, 51–66.

646 Suszyńska, M., Krajczyk, L., and Mazurkiewicz, Z. (2003) TEM studies of silver nanoparticles
647 in phase-separated soda lime silicate glasses. Materials Chemistry and Physics, 81, 404–
648 406.

649 Suszyńska, M., Morawska-Kowal, T., and Krajczyk, L. (2010) Optical properties of small silver
650 particles embedded in soda-lime silica glasses. Optica Applicata, 40, 397–401.

651 Wang, C., Shen, A.H., Palke, A.C., and Heaney, P.J. (2019) Color origin of the Oregon sunstone
652 pp. 71–74. Presented at the 36th International Gemmological Conference IGC, Nantes
653 France.

654 Wriedt, T. (2009) Light scattering theories and computer codes. Journal of Quantitative
655 Spectroscopy and Radiative Transfer, 110, 833–843.

656 Xu, H., Hill, T.R., Konishi, H., and Farfan, G. (2017) Protoenstatite: A new mineral in Oregon
657 sunstones with “watermelon” colors. American Mineralogist, 102, 2146–2149.

Figure 1 Schematic diagram illustrating light interaction with nanoparticles in a colloid suspension. The wavy lines represent the energy absorbed by the particles and dissipated as heat. It is impossible to measure absorption independently, only the total extinction (absorption + scattering) can be calculated from transmittance. All published absorption spectra are actually extinction spectra by assuming zero scattering. The scattered light in any particular direction may be imperceptible, but the total scattering (all directions combined) can have a significant extinction effect.

Figure 2 Coordinates used for calculation defined relative to the spheroid, along with the orientations of the three linearly polarized incident light. Because of the rotational symmetry of the spheroid along the Z-axis, the effect of the incident light would not change with any rotation around the Z-axis. Therefore, the three orientations of incident light can be unambiguously described as K_z, M_z and E_z.

Figure 3 The absorption, scattering and extinction power of spherical particles plotted against wavelength and radius. The color map is plotted in log scale for easy comparison. The same color map in linear color scale can be found in Figure S1 in Supplementary Material for better contrast.

Figure 4 The absorption, scattering and extinction power plotted against wavelength (400 nm - 1000 nm) and aspect ratio ($0.5 < \frac{\boldsymbol{c}}{\boldsymbol{a}} < 2$) of spheroid Cu particles with equatorial radius $\boldsymbol{a}$ = 35 nm for all three incident light orientations. The same log color scale as Figure 3 is used.

Figure 5 The absorption, scattering and extinction power, of three incident light orientations, plotted against wavelength (400 nm – 1000 nm) and equatorial radius (0 – 100 nm) for oblate Cu spheroid with $\frac{\boldsymbol{c}}{\boldsymbol{a}} = 0.5$. The same log color scale as Figure 3 and 4 is used.

Figure 6 The absorption, scattering and extinction power, of three incident light orientations, plotted against wavelength (400 nm – 1000 nm) and equatorial radius (0 – 100 nm) for prolate Cu spheroid with $\frac{\boldsymbol{c}}{\boldsymbol{a}} = 2$. The same log color scale as Figure 3, 4 and 5 is used.

Figure 7 The phase functions $F(\theta, \varphi)$ (normalized intensity of scattered light at a given direction) of spherical particles with radius of 60, 80 and 100 nm for λ = 600 nm, plotted as enclosed surfaces in spherical coordinates. The direction and polarization plane of the incident light are marked with red arrows and purple planes. The vertical red plane separates the forward scattered light from the backscattered light. Note that the surface is plotted as $3\sqrt[3]{F(\theta, \varphi)}$, so that the scattered energy is represented by the volume of the cone in a given direction (apex at the origin), instead of the distance from the surface to

691 the origin. The total enclosed volume of the surface is therefore always 1. For $R \ll \lambda$, the
692 light is scattered evenly along all directions (perpendicular to polarization). The scattered
693 intensity shifts towards the forward direction with increasing size of the particle.

694 Figure 8 The calculated extinction (attenuation) spectrum of a Cu-colored labradorite crystal
695 containing 10ppm of spherical Cu particles of radius of 5 nm, which is the sum of the
696 absorption spectrum of sample DD-012 (Cu-free labradorite) and the calculated
697 extinction spectrum of the Cu particle. The orientation dependence of the Fe^{3+} absorption
698 band in feldspar is insignificant (Hofmeister and Rossman 1983, 1984), therefore
699 neglected in this study.

700 Figure 9 The calculated color of Cu-sunstones (3mm thick with 20 ppmw of Cu particles) plotted
701 against the aspect ratio ($0.5 < \frac{c}{a} < 2$) and the equatorial radius (0 nm < $\boldsymbol{a}$ < 100 nm) of
702 the Cu spheroids, with linearly polarized incident light (M_Z and E_Z). Color with
703 unpolarized light is also calculated by averaging the attenuance of the two perpendicular
704 polarizations.

705 Figure 10 Measured polarized extinction spectra of the four Cu-sunstone samples, (*a*) SB-001,
706 (*b*) A110, (*c*) A112 and (*d*) A090, along with the images of the samples under
707 transmission light with the same polarization. The spectra for maximum and minimum
708 extinction are plotted in dotted and solid lines respectively. The spectra are measured in
709 the areas with green color (at maximum extinction).

710 Figure 11 Sample A110 (Figure 10*b*) under plane polarized transmission light (*a*), (*b*) and
711 reflective light (*c*), (*d*). The polarization directions are marked with cyan arrows. The
712 pleochroic area of the crystal [green area in (b)] scatters back strongly polarized red light
713 matching the extinction under transmission light (stronger backscattering with
714 polarization of maximum extinction).

715 Figure 12 The scattered intensity (energy density) by a Cu sphere with a radius of 2μm plotted
716 against wavelength and scattering angle. Around 50% of the total scattered energy are
717 diffracted within 5° of the forward direction ($\theta < 5°$), and the rest of the scattered energy
718 is almost evenly distributed in all the other directions. For scattering angle larger than
719 30°, the scattered energy shows a sharp increase around 560 nm, with the longer
720 wavelengths scattered about twice as intense as the shorter wavelengths.

This is the peer-reviewed, final accepted version for American Mineralogist, published by the Mineralogical Society of America.
The published version is subject to change. Cite as Authors (Year) Title. American Mineralogist, in press.
DOI: https://doi.org/10.2138/am-2022-8325. http://www.minsocam.org/

741 Table 1 Chemical formula of the major feldspar elements normalized to 4 (Al + Si) from the LA-
742 ICP-MS results.

	Ca	**Na**	**K**	**Al**	**Si**	**Composition**
DD-012	0.648	0.334	0.007	1.643	2.357	$An_{65.5}Ab_{33.8}Or_{0.7}$
	0.641	0.331	0.007	1.643	2.357	$An_{65.5}Ab_{33.8}Or_{0.7}$
SB-001	0.688	0.312	0.006	1.660	2.340	$An_{68.3}Ab_{31.0}Or_{0.6}$
	0..671	0.312	0.006	1.648	2.352	$An_{67.9}Ab_{31.5}Or_{0.6}$
A110	0.467	0.478	0.028	1.474	2.526	$An_{48.0}Ab_{49.2}Or_{2.8}$
	0.472	0.480	0.027	1.454	2.546	$An_{48.2}Ab_{49.0}Or_{2.8}$
A112	0.449	0.501	0.030	1.419	2.581	$An_{45.8}Ab_{51.1}Or_{3.1}$
	0.444	0.496	0.030	1.412	2.588	$An_{45.8}Ab_{51.1}Or_{3.1}$
A090	0.460	0.480	0.027	1.474	2.526	$An_{47.6}Ab_{49.6}Or_{2.8}$
	0.471	0.475	0.027	1.460	2.540	$An_{48.4}Ab_{48.8}Or_{2.8}$

743

744 Table 2 Concentrations of selected trace elements from the LA-ICP-MS in ppmw. The limit of
745 detection for each element is listed below the element.

	Li *0.113*	**Mg** *0.032*	**P** *1.304*	**Ti** *0.146*	**Mn** *0.021*	**Fe** *0.704*	**Cu** *0.015*	**Ga** *0.003*	**Sr** *0.001*	**Ba** *0.002*	**Pb** *0.002*
DD-012	2.04	840	23.9	230	41.8	3096	0.46	16.9	642	65.5	0.17
	2.02	835	27.3	232	41.8	3091	0.30	17.0	628	65.4	0.17
SB-001	19.1	891	28.3	259	49.2	3537	47	17.2	590	62.4	0.15
	18.9	906	29.3	249	46.9	3407	49	16.7	580	63.2	0.15
A110	29.9	465	50.7	406	29.8	2622	677	19.9	1115	140	0.41
	29.7	468	51.6	402	30.4	2619	667	19.8	1101	138	0.40
A112	10.8	452	51.7	408	30.3	2658	501	19.9	1064	142	0.44
	11.4	423	55.8	412	30.1	2635	511	20.0	1062	148	0.45
A090	15.7	445	53.4	392	29.0	2539	470	19.8	1094	134	0.47
	15.0	456	52.0	403	30.0	2635	468	20.1	1120	142	0.41

This is the peer-reviewed, final accepted version for American Mineralogist, published by the Mineralogical Society of America.
The published version is subject to change. Cite as Authors (Year) Title. American Mineralogist, in press.
DOI: https://doi.org/10.2138/am-2022-8325. http://www.minsocam.org/

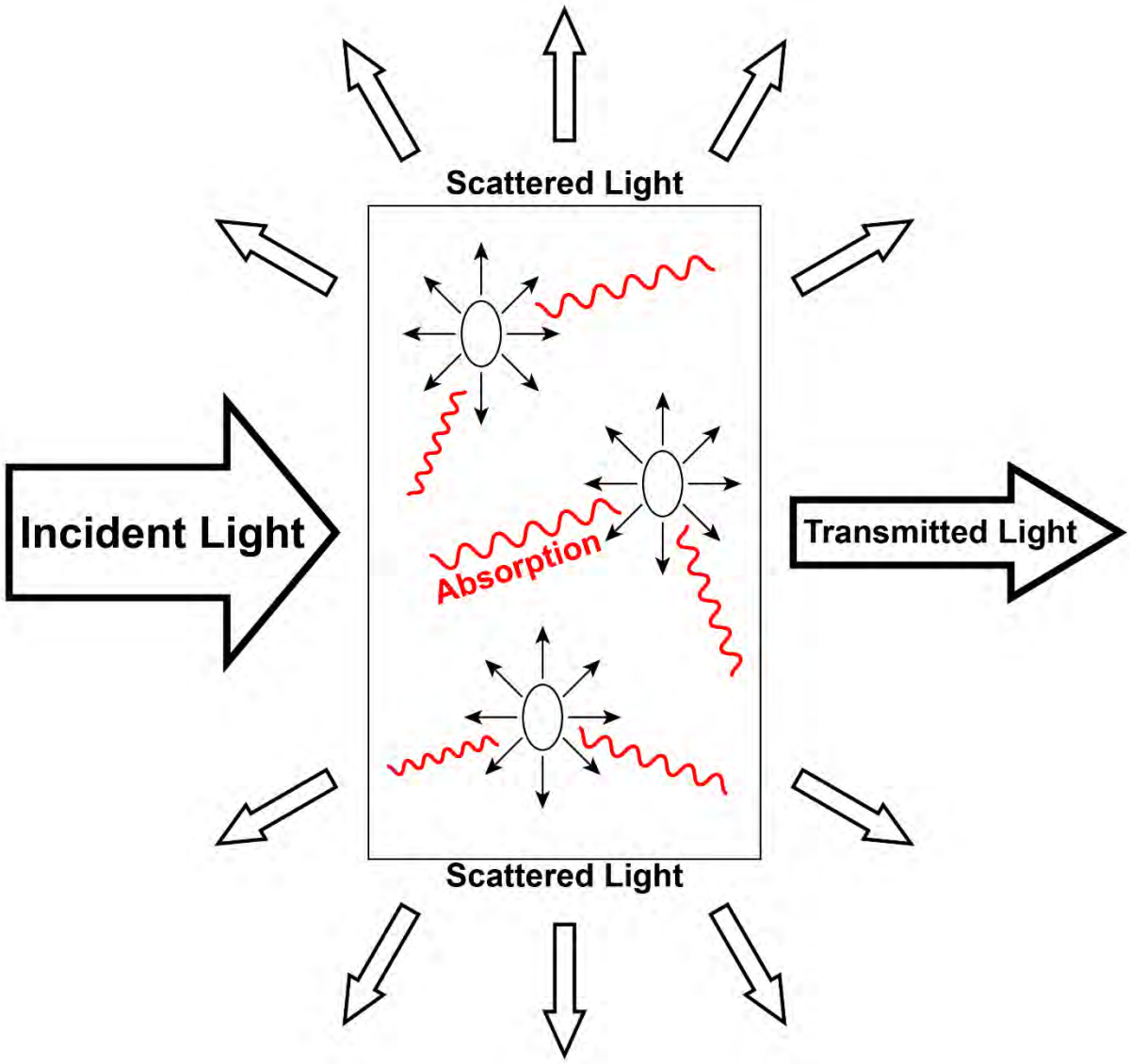

746
747 Figure 1

This is the peer-reviewed, final accepted version for American Mineralogist, published by the Mineralogical Society of America.
The published version is subject to change. Cite as Authors (Year) Title. American Mineralogist, in press.
DOI: https://doi.org/10.2138/am-2022-8325. http://www.minsocam.org/

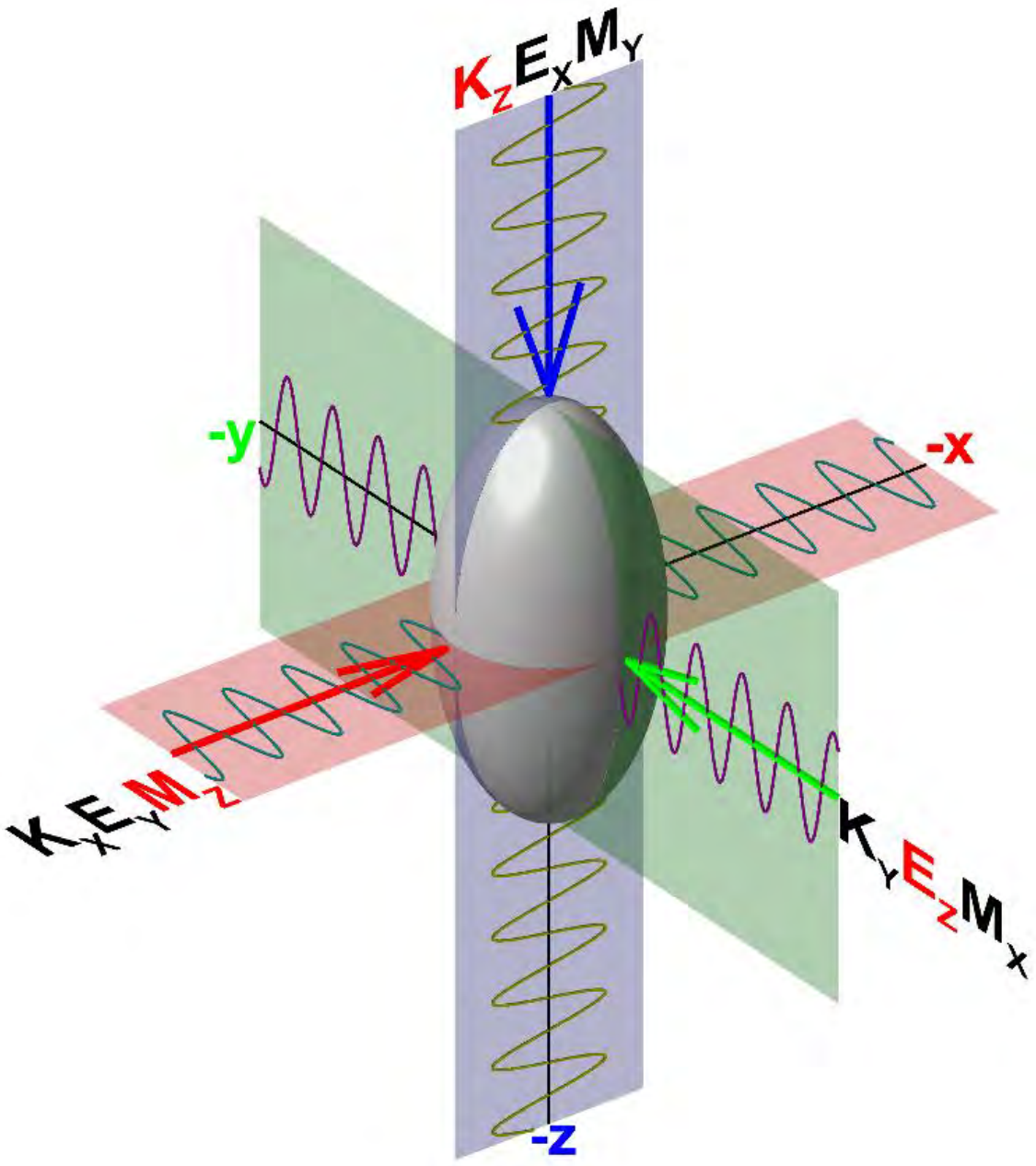

748
749 Figure 2

This is the peer-reviewed, final accepted version for American Mineralogist, published by the Mineralogical Society of America.
The published version is subject to change. Cite as Authors (Year) Title. American Mineralogist, in press.
DOI: https://doi.org/10.2138/am-2022-8325. http://www.minsocam.org/

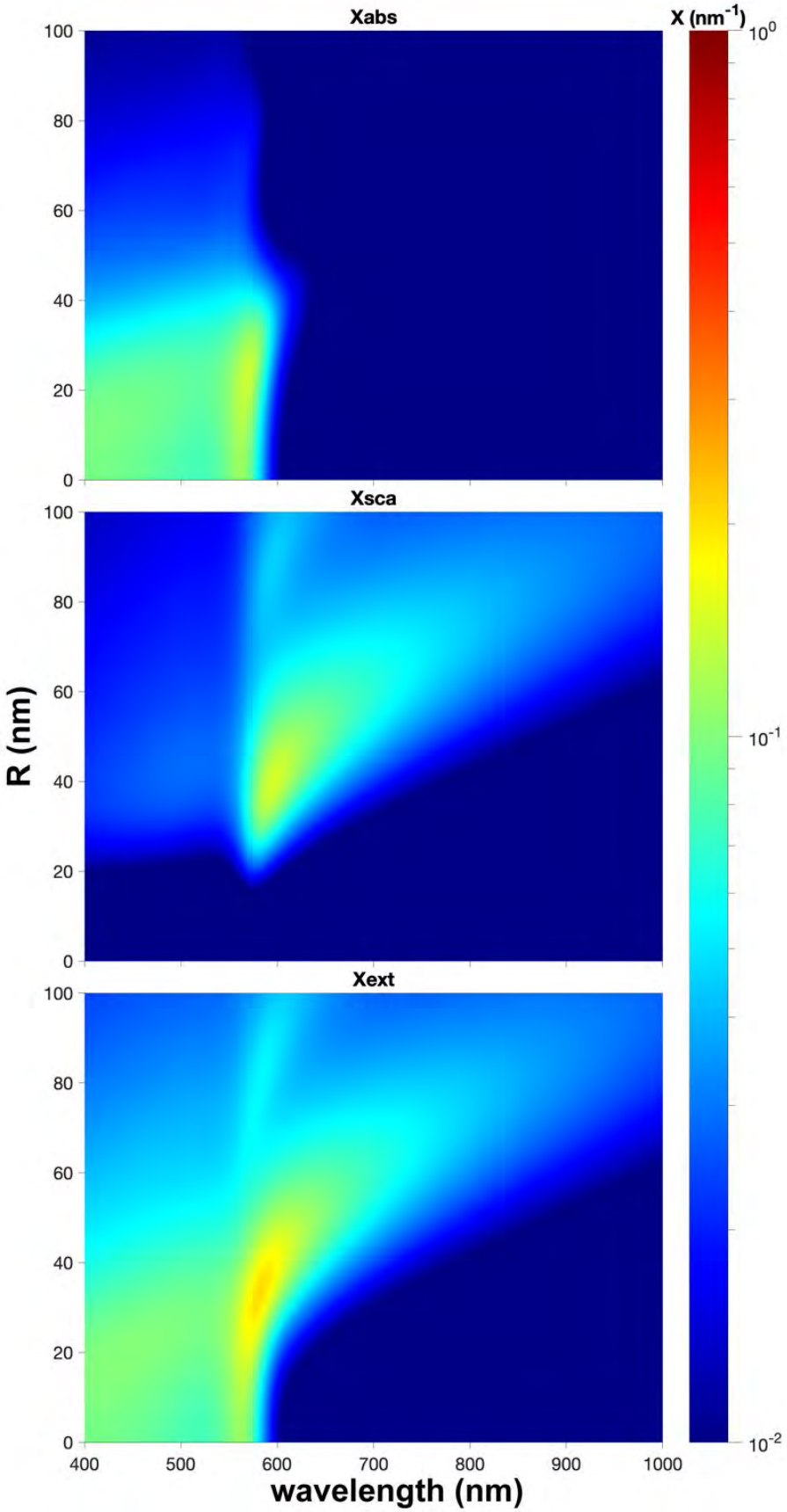

750

Figure 3

This is the peer-reviewed, final accepted version for American Mineralogist, published by the Mineralogical Society of America.
The published version is subject to change. Cite as Authors (Year) Title. American Mineralogist, in press.
DOI: https://doi.org/10.2138/am-2022-8325. http://www.minsocam.org/

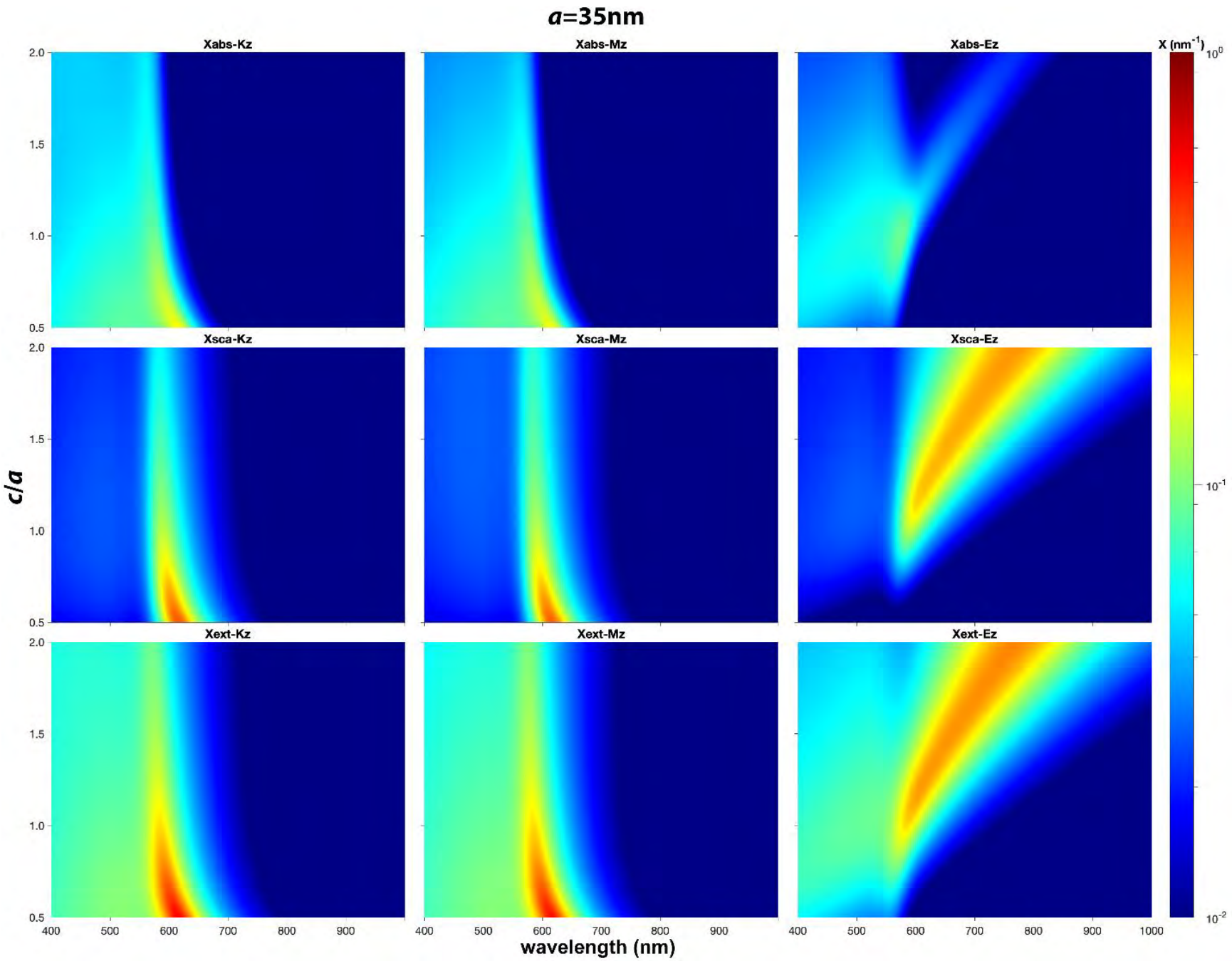

751
752 Figure 4

This is the peer-reviewed, final accepted version for American Mineralogist, published by the Mineralogical Society of America.
The published version is subject to change. Cite as Authors (Year) Title. American Mineralogist, in press.
DOI: https://doi.org/10.2138/am-2022-8325. http://www.minsocam.org/

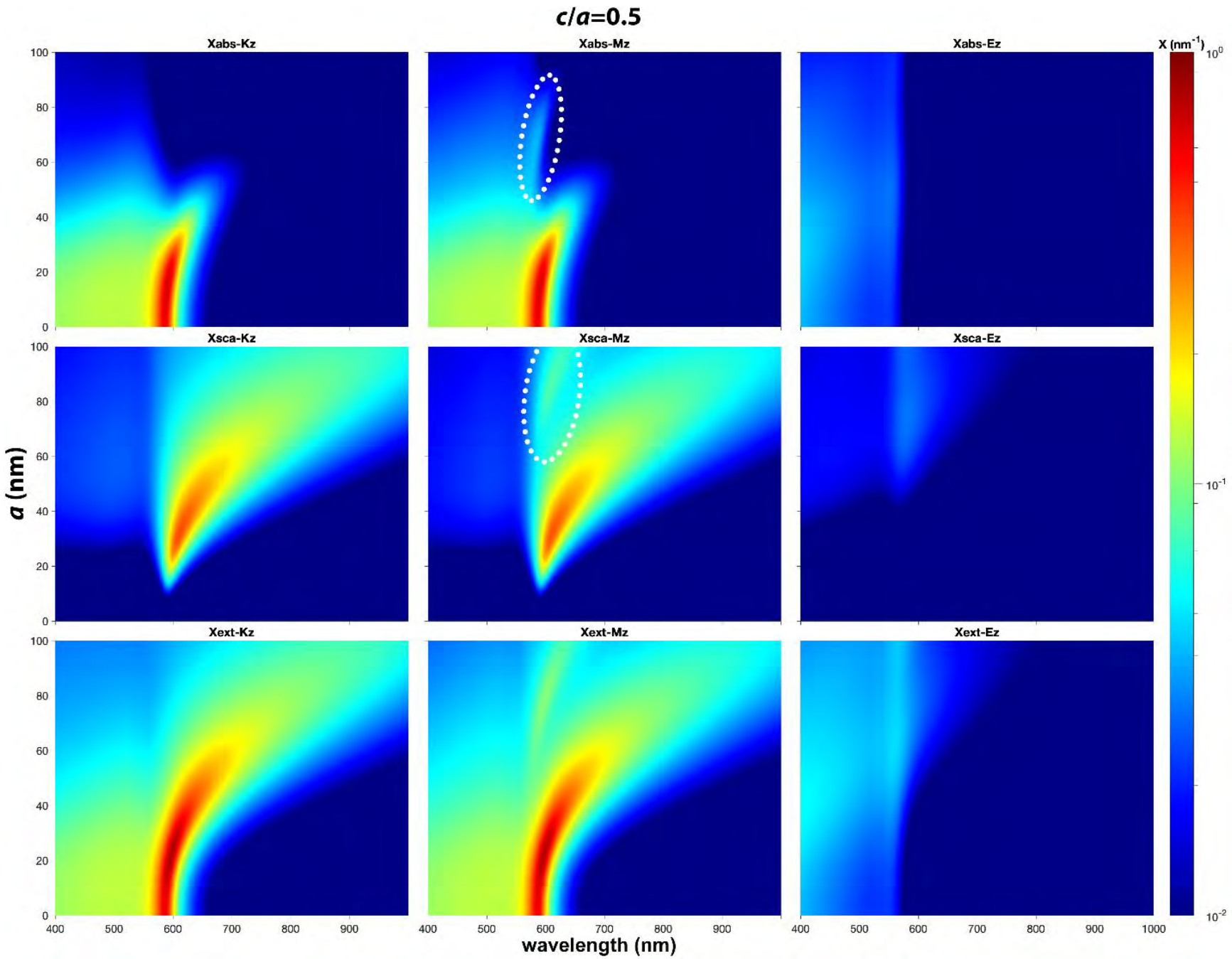

753
754 Figure 5

This is the peer-reviewed, final accepted version for American Mineralogist, published by the Mineralogical Society of America.
The published version is subject to change. Cite as Authors (Year) Title. American Mineralogist, in press.
DOI: https://doi.org/10.2138/am-2022-8325. http://www.minsocam.org/

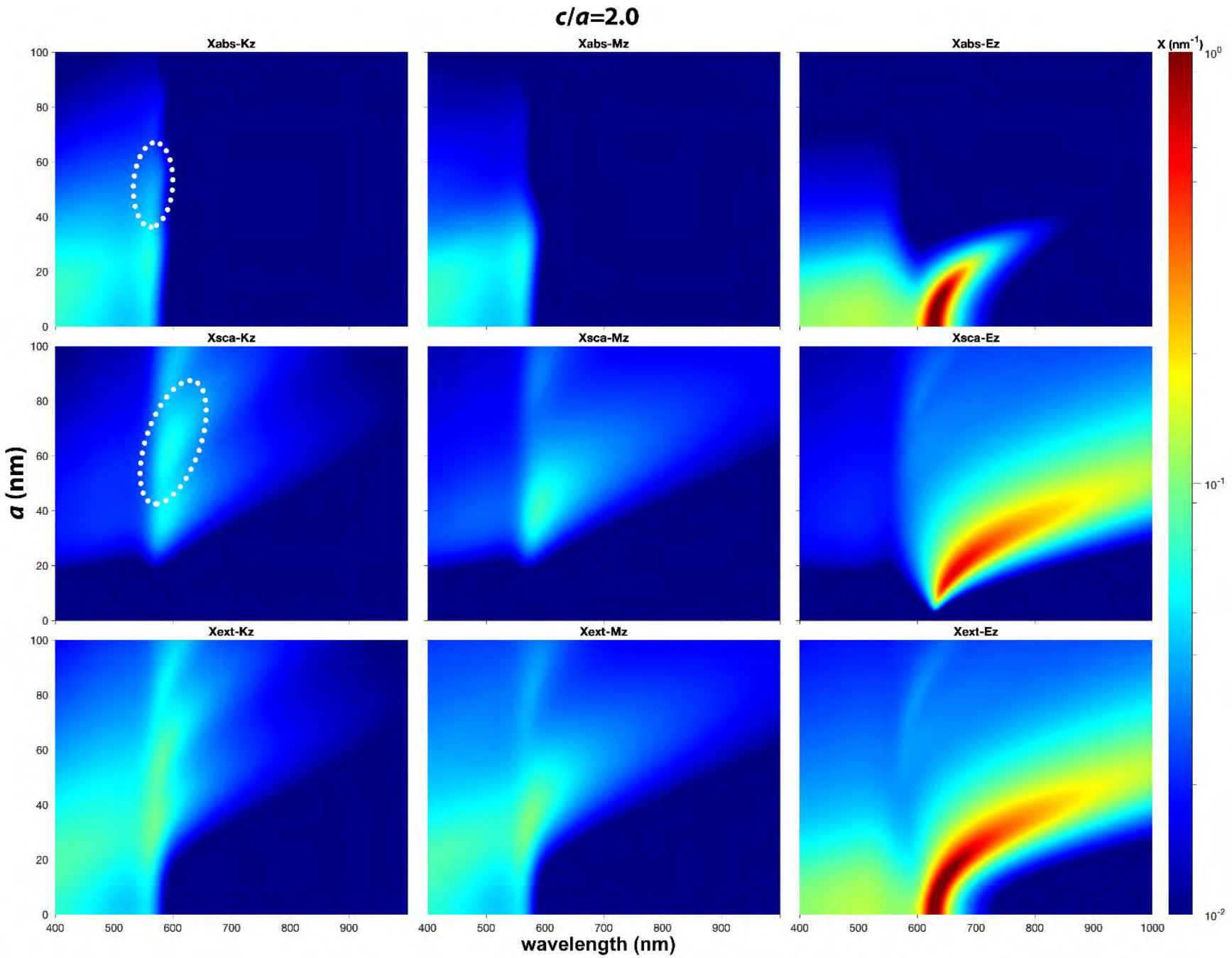

Figure 6

This is the peer-reviewed, final accepted version for American Mineralogist, published by the Mineralogical Society of America.
The published version is subject to change. Cite as Authors (Year) Title. American Mineralogist, in press.
DOI: https://doi.org/10.2138/am-2022-8325. http://www.minsocam.org/

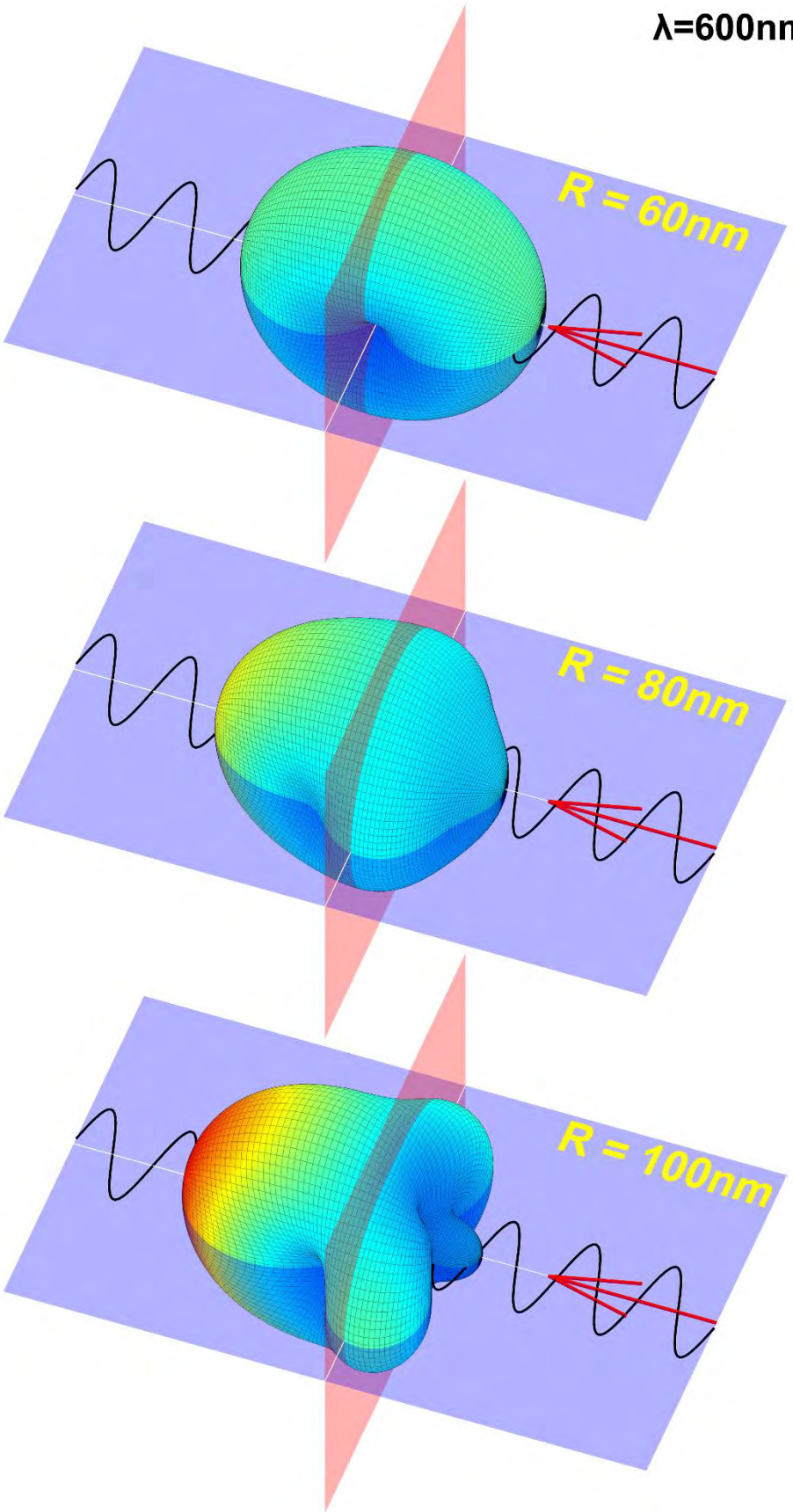

757

Figure 7

This is the peer-reviewed, final accepted version for American Mineralogist, published by the Mineralogical Society of America.
The published version is subject to change. Cite as Authors (Year) Title. American Mineralogist, in press.
DOI: https://doi.org/10.2138/am-2022-8325. http://www.minsocam.org/

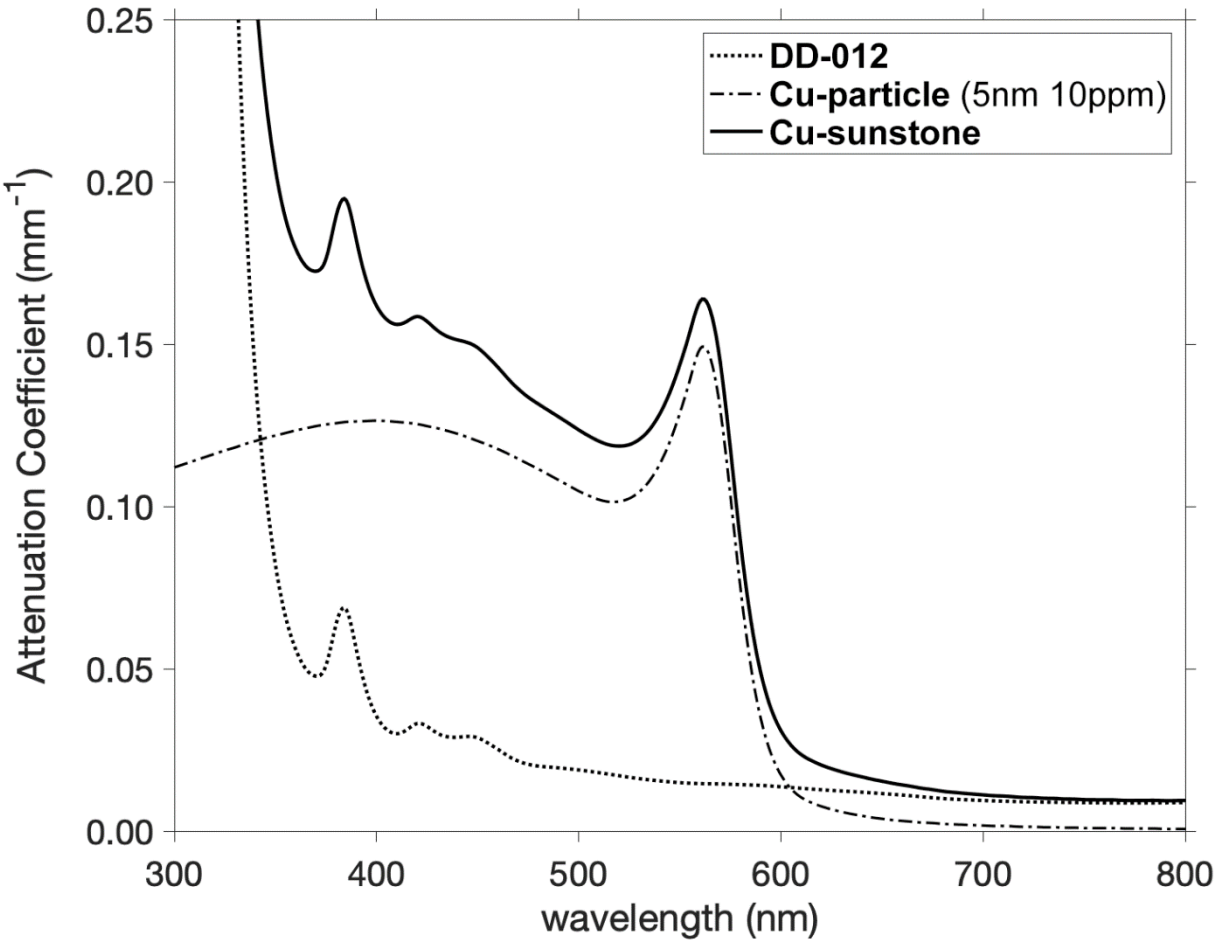

Figure 8

This is the peer-reviewed, final accepted version for American Mineralogist, published by the Mineralogical Society of America.
The published version is subject to change. Cite as Authors (Year) Title. American Mineralogist, in press.
DOI: https://doi.org/10.2138/am-2022-8325. http://www.minsocam.org/

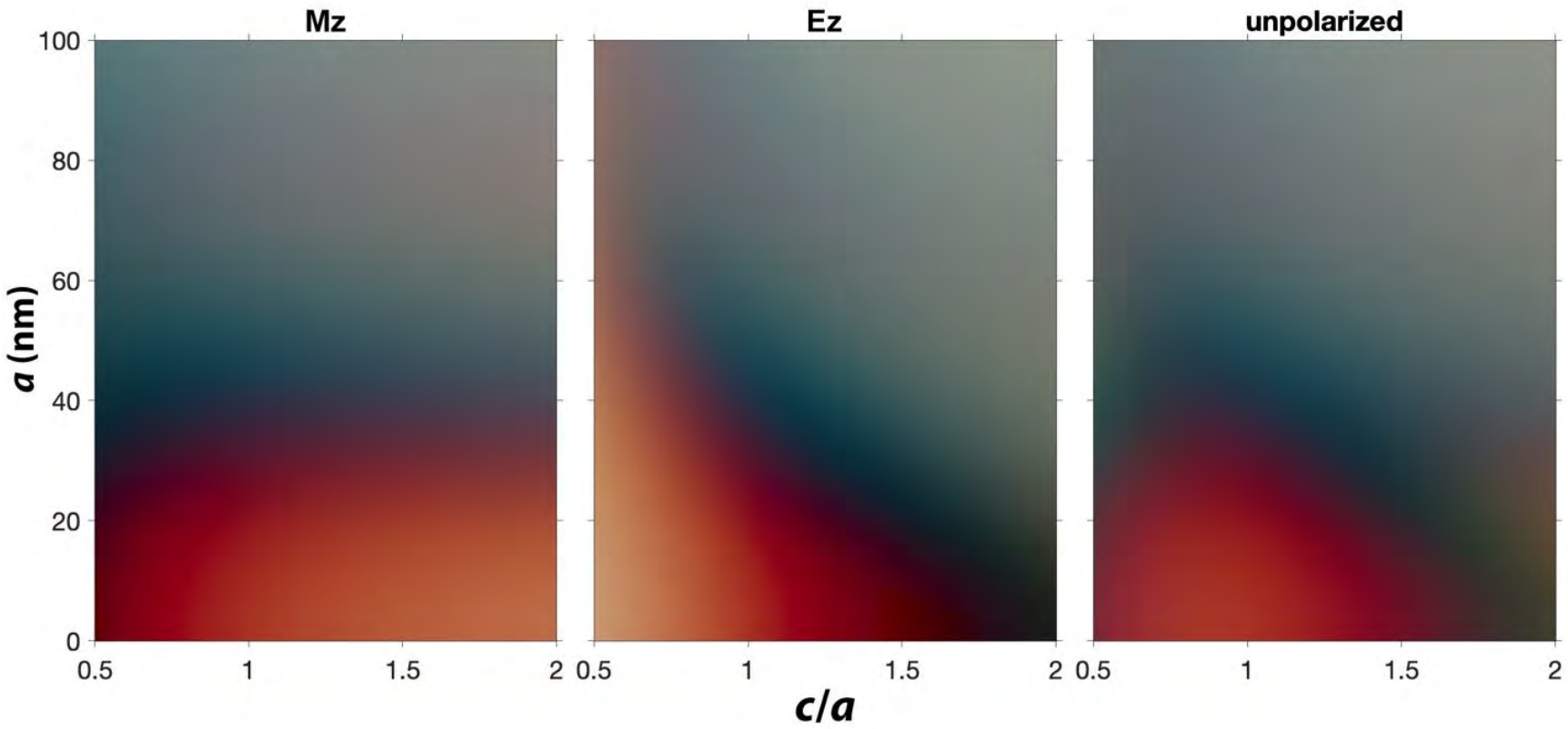

Figure 9

This is the peer-reviewed, final accepted version for American Mineralogist, published by the Mineralogical Society of America.
The published version is subject to change. Cite as Authors (Year) Title. American Mineralogist, in press.
DOI: https://doi.org/10.2138/am-2022-8325. http://www.minsocam.org/

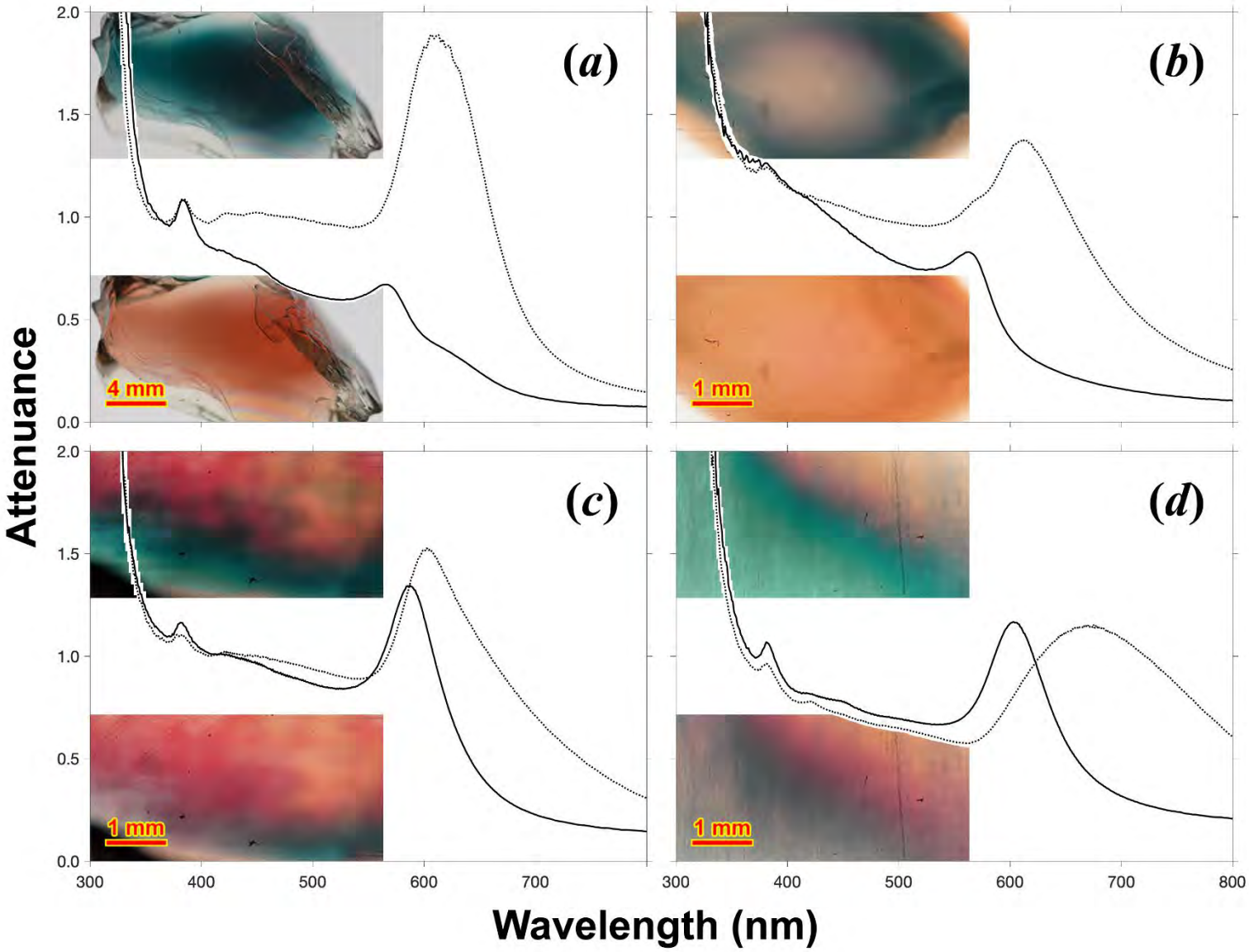

762
763 Figure 10

This is the peer-reviewed, final accepted version for American Mineralogist, published by the Mineralogical Society of America.
The published version is subject to change. Cite as Authors (Year) Title. American Mineralogist, in press.
DOI: https://doi.org/10.2138/am-2022-8325. http://www.minsocam.org/

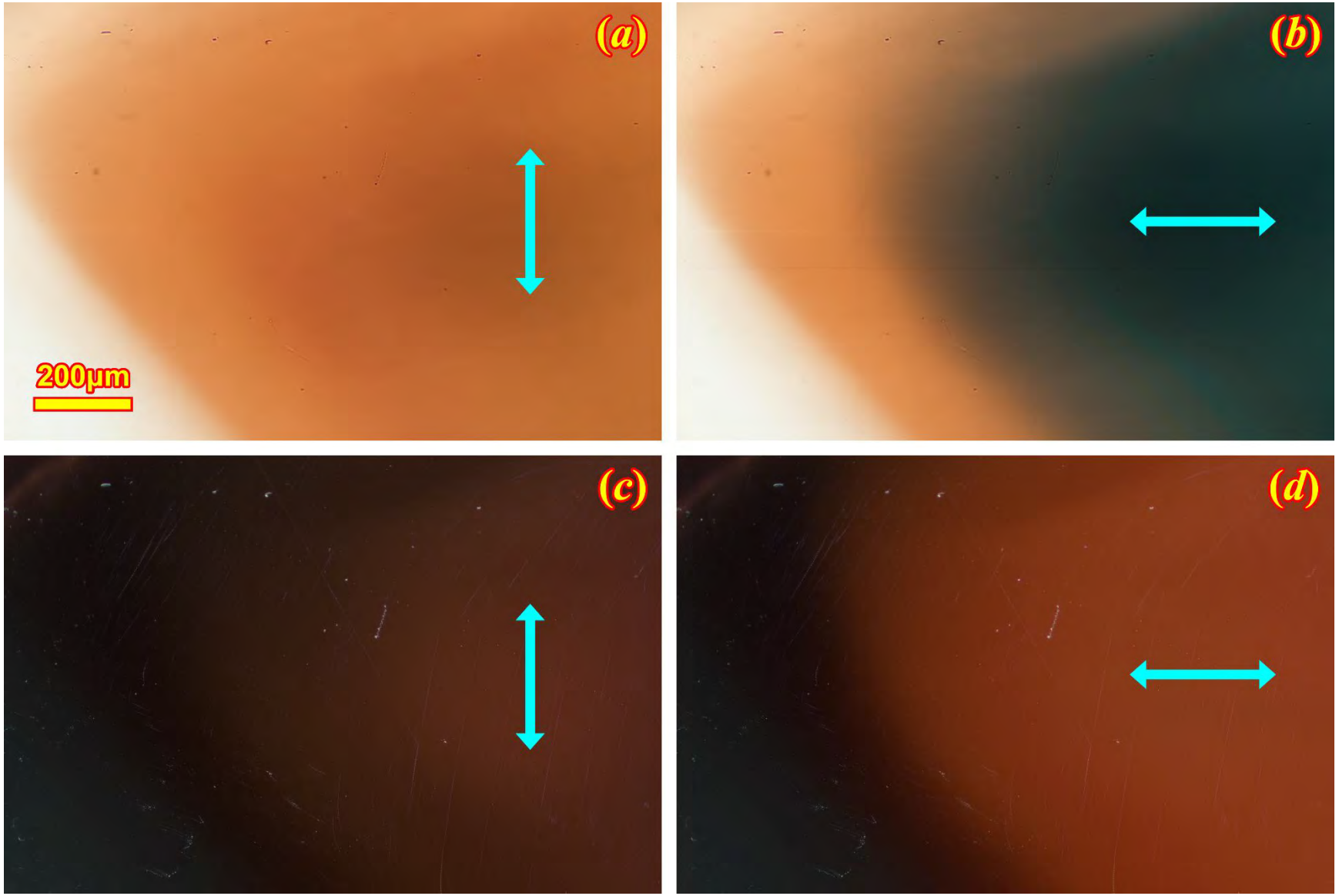

Figure 11

This is the peer-reviewed, final accepted version for American Mineralogist, published by the Mineralogical Society of America.
The published version is subject to change. Cite as Authors (Year) Title. American Mineralogist, in press.
DOI: https://doi.org/10.2138/am-2022-8325. http://www.minsocam.org/

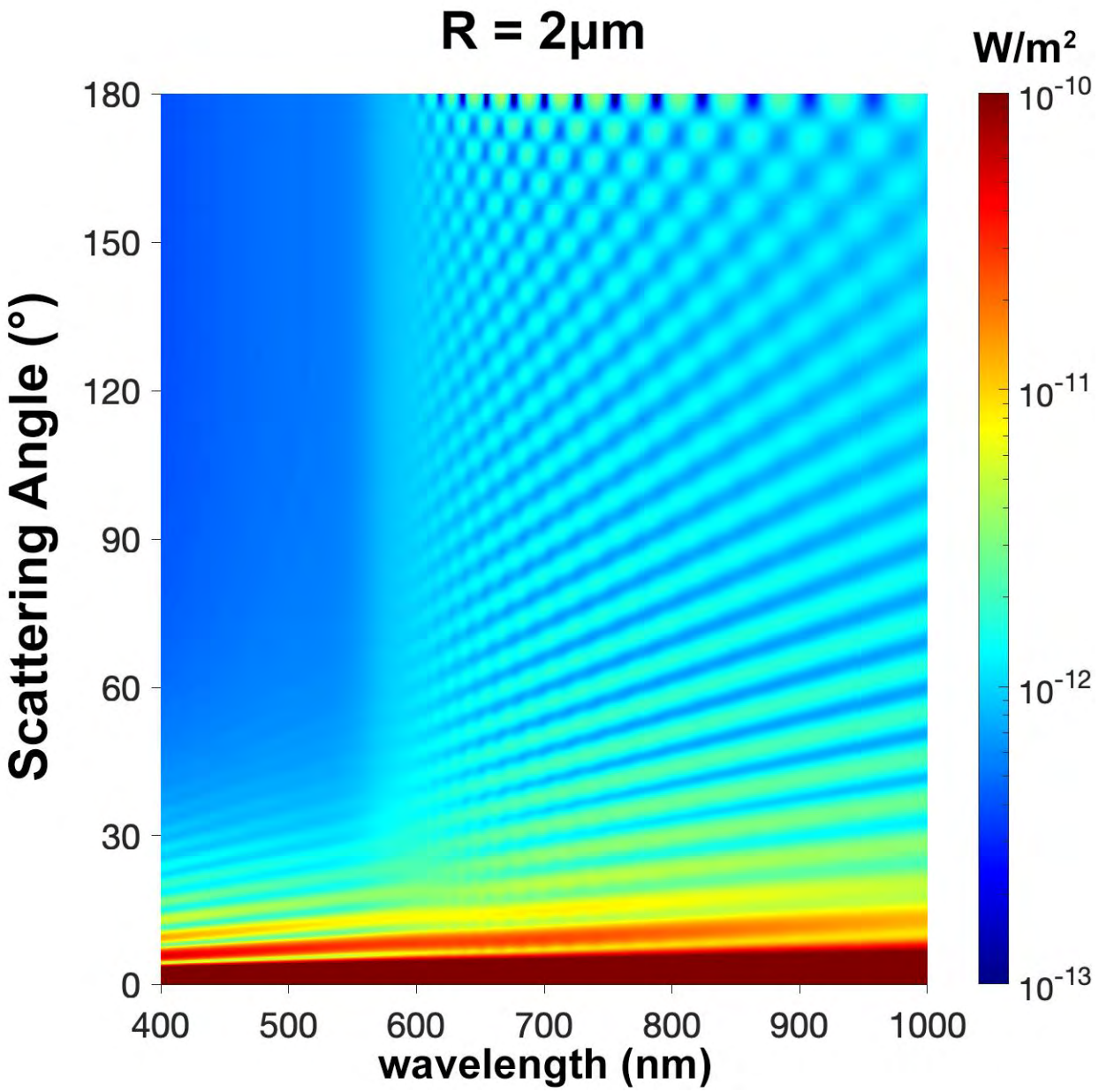

Figure 12